

# Synergy between palladium single atoms and small nanoparticles co-anchored on carbon atom self-doped graphitic carbon nitride boosting photocatalytic H<sub>2</sub> generation

Miao Ren, Jiaqi Meng, Yuxin Yang, Xueyan Zhang, Guang Yang, Lang Qin, Yihang Guo <sup>\*</sup>

*School of Environment, Northeast Normal University, Changchun 130117, PR China*



## ARTICLE INFO

### Keywords:

Photocatalysis  
Hydrogen evolution reaction  
Graphitic carbon nitride  
Single atom  
Palladium

## ABSTRACT

Supramolecule self-assembly of dicyandiamide and uracil followed by thermal polymerization route is designed to prepare carbon atom self-doped g-C<sub>3</sub>N<sub>4</sub> (CCN<sub>x</sub>), and then wet reduction is applied to fabricate Pd single atoms (Pd<sub>1</sub>) and nanoparticles (Pd<sub>NPs</sub>) co-anchored CCN<sub>x</sub> heterojunctions (Pd<sub>1+NPs</sub>/CCN<sub>x</sub>). In Pd<sub>1+NPs</sub>/CCN<sub>x</sub> structure, interlayer Pd–N<sub>4</sub> coordination is the most favorable for chemically stabilizing Pd<sub>1</sub>, while Pd<sub>NPs</sub> accumulate on the in-plane of CCN<sub>x</sub>. Pd<sub>1+NPs</sub>/CCN<sub>x</sub> heterojunctions exhibit remarkably enhanced photocatalytic H<sub>2</sub> evolution reaction (HER) activity, and HER rate and AQY value reach up to 24.1 mmol g<sup>-1</sup> h<sup>-1</sup> and 17.1% (400 nm) over the optimized Pd<sub>1+NPs</sub>/CCN<sub>x</sub> catalyst. Mechanism studies unveil that synergy of as-built interlayer N–Pd–N electron transfer channels at the atomic-scale and surface Mott–Schottky effect of small Pd nanoparticles notably accelerates migration of photogenerated electrons, which leads to plentiful electrons accumulation around Pd single atoms and small nanoparticles to decrease the energy barrier of H<sup>\*</sup> activation and boost HER photodynamics significantly.

## 1. Introduction

Hydrogen (H<sub>2</sub>) is an important secondary energy resource due to its zero-carbon emission and high gravimetric energy density. Among various advanced H<sub>2</sub> production technologies, solar-driven photocatalytic water splitting holds particular attention and shows great potential for the cost-effective large-scale production of green H<sub>2</sub> energy [1–3]. Designing efficient H<sub>2</sub> production photocatalysts and unveiling H<sub>2</sub> evolution reaction (HER) mechanism are still the hot topics in this field. Notwithstanding tremendous efforts have been devoted, it still remains significant challenges to accomplish efficient photocatalytic water splitting for H<sub>2</sub> production due to fast photogenerated electron–hole recombination and limited light utilization efficiency. In pursuit of robust H<sub>2</sub> production photocatalysts, graphitic carbon nitride (g-C<sub>3</sub>N<sub>4</sub>) has attracted great interest [4]. As an earth-abundant element-based π-conjugated polymeric semiconductor photocatalyst, g-C<sub>3</sub>N<sub>4</sub> exhibits unique advantages over the inorganic counterparts, which include visible-light response and strong light harvesting capacity; more importantly, flexible molecular structure renders g-C<sub>3</sub>N<sub>4</sub> easily adjustable electronic structures and band structures through versatile molecular engineering strategies, which provide lots of new

opportunities to develop g-C<sub>3</sub>N<sub>4</sub>-based photocatalysts for highly efficient H<sub>2</sub> production [5,6]. Thermodynamically, g-C<sub>3</sub>N<sub>4</sub> is a suitable solar-driven H<sub>2</sub> production photocatalyst with bandgap of ca. 2.7 eV and CB edge potential of –1.3 V (vs. NHE) [7–10]. Nevertheless, high symmetry of the planar structure endows the uniform distribution of electrons on LUMO and holes on HOMO in g-C<sub>3</sub>N<sub>4</sub>, which results in sluggish internal charge transport photodynamics and thus high electron-hole recombination probability. To improve solar-to-H<sub>2</sub> conversion efficiency, boosting fast charge carrier separation and transport dynamics is a primary issue. Among various emerging modification strategies, defect engineering by the introduction of vacancies or dopants to heptazine rings of g-C<sub>3</sub>N<sub>4</sub>, as an atomic-level structure regulation strategy, is an effective and attractive way to adjust atomic composition and electronic states by breaking the structural symmetry. The asymmetric charge carrier distribution within defect-modified g-C<sub>3</sub>N<sub>4</sub> framework can induce the generation of a local electric field to facilitate the directional migration of charge carriers and thereby notably enhanced solar-to-H<sub>2</sub> conversion efficiency [11–15]. On the other hand, to increase the number of the active sites for HER, noble metal (e.g., Pt or Pd) nanoparticles as cocatalyst to capture the photogenerated electrons are essential. However, high cost and finite reserves restrict the

\* Corresponding author.

E-mail address: [guoyh@nenu.edu.cn](mailto:guoyh@nenu.edu.cn) (Y. Guo).

application of noble metal in large scale H<sub>2</sub> production. Benefiting from the maximum atom utilization efficiency and well-distributed active sites with tunable electronic environment, light-harvesting semiconductor-immobilized single noble metal atoms have attracted great attention for HER more recently [16–18]. For the fabrication of g-C<sub>3</sub>N<sub>4</sub>-immobilized single noble metal atom photocatalysts, defect-modified g-C<sub>3</sub>N<sub>4</sub> demonstrate superior advantage to its pristine counterpart. Defects can create new and powerful coordination unsaturated centers around sp<sup>2</sup>-bonded N atoms in heptazine rings, which provide abundant active sites for chemically anchoring and stabilizing noble metals through the formation of noble metal M–N coordination bonds. This is an essential prerequisite to constructing stable single noble metal atom catalysts with relatively high density; moreover, the formation of M–N coordination bonds builds a robust and new electron transport path at an atomic-level, which greatly facilitate electron transport dynamics to single noble metal atoms [19]. Hence, defect-modified g-C<sub>3</sub>N<sub>4</sub> is an ideal photocatalytically active support for the immobilization of single noble metal atoms to remarkably improve HER activity.

To address the above full considerations, herein, an *in situ* self-doping modification approach is developed to prepare C atom self-doped g-C<sub>3</sub>N<sub>4</sub> by selecting dicyandiamide as a C/N monomer and π-electron-rich small organic molecule (i.e., uracil) as a precursor of foreign C atoms. The preparation process includes supramolecule self-assembly of dicyandiamide and uracil to hydrogen-bonded supramolecular aggregate followed by thermal copolymerization. In comparison of direct thermal copolymerization of dicyandiamide and uracil to C atom self-doped g-C<sub>3</sub>N<sub>4</sub> [20], the above supramolecule self-assembly is a crucial preorganization step to optimize the molecular structure of defect-modified g-C<sub>3</sub>N<sub>4</sub>; meanwhile, C doping level or the concentration of the defect is controllable by adjusting uracil-to-dicyandiamide molar ratio. As a result, the electronic structure and band structure of g-C<sub>3</sub>N<sub>4</sub> are adjusted precisely. Subsequently, a facile approach of low-temperature hydrothermal treatment of C atom self-doped g-C<sub>3</sub>N<sub>4</sub> (represented by CCN<sub>x</sub>, and “x” refers to CCN<sub>x</sub> obtained at different uracil-to-dicyandiamide molar ratios) and PdCl<sub>2</sub> in ethylene glycol system is designed to introduce Pd species to CCN<sub>x</sub>. Interestingly, except for the formation of atomically dispersed Pd species (Pd<sub>1</sub>) in CCN<sub>x</sub> framework, certain small Pd nanoparticles (Pd<sub>NPs</sub>) are also co-anchored on CCN<sub>x</sub>. By combination of advanced characterizations with density functional theory (DFT) calculations, the rational chemical structure of as-prepared Pd<sub>1+NPs</sub>/CCN<sub>x</sub> heterojunctions is proposed, in which interlayer Pd–N<sub>4</sub> coordination configuration is the most favorable for the spatial isolation of Pd species to form Pd<sub>1</sub>, while the rest of Pd species agglomerate to small Pd<sub>NPs</sub> that inhabit on the in-plane of CCN<sub>x</sub>. Pd<sub>1+NPs</sub>/CCN<sub>x</sub> heterojunctions exhibit significantly enhanced photocatalytic HER activity, outperforming the reference catalysts including Pd<sub>NPs</sub>/CN, Pd<sub>NPs</sub>/CCN<sub>x</sub> and Pd<sub>NPs</sub>/CCN<sub>x'</sub> prepared by immobilization of Pd species on bulk g-C<sub>3</sub>N<sub>4</sub>, NaBH<sub>4</sub> reduction of Pd species in CCN<sub>x</sub> system and immobilization of Pd species on CCN<sub>x'</sub> supports obtained by direct thermal copolymerization of dicyandiamide and uracil, respectively. By analyzing the results of extensive characterizations (especially *in situ* femtosecond time-resolved transient absorption spectroscopy) and theoretical simulation, photocatalytic HER mechanism over Pd<sub>1+NPs</sub>/CCN<sub>x</sub> is studied in-depth. It is revealed that the synergy between Pd<sub>1</sub> and small Pd<sub>NPs</sub> both as the electron-trapping sites significantly decrease the energy barrier of activation of H<sup>\*</sup> and remarkably boost charge carrier transport dynamics, creating plentiful long-lived free photogenerated electrons to notably enhance HER activity.

## 2. Experimental

### 2.1. Catalyst Preparation

Pd<sub>1+NPs</sub>/CCN<sub>x</sub> heterojunctions was prepared as follows. Uracil (0.067, 0.10, 0.20 and 0.40 g, respectively) was dissolved in water (30

mL), and dicyandiamide (10.0 g) was dispersed in water (30 mL). As-formed uracil solution was added to dicyandiamide suspension, and the obtained mixture was stirred for 2 h at room temperature. The mixture was then transferred to an autoclave and heated to 180 °C for 10 h. Afterwards, the collected white powder was washed by water until the effluent became neutral, and melamine-cyanuric acid-uracil supramolecular aggregate (MCUS) was thus obtained after being dried. Further calcination of MCUS at 550 °C for 3 h at a heating ramp of 3 °C min<sup>-1</sup> under N<sub>2</sub> flow produced CCN<sub>x</sub>, in which x = 1, 2, 3 and 4, and the resulting CCN<sub>1</sub>, CCN<sub>2</sub>, CCN<sub>3</sub> and CCN<sub>4</sub> corresponded to CCN<sub>x</sub> prepared at uracil-to-dicyandiamide molar ratio of 0.005, 0.0075, 0.015 and 0.030, respectively. Subsequently, CCN<sub>x</sub> (100 mg) was dispersed in 16 mL ethylene glycol (EG) solution, and then PdCl<sub>2</sub> solution (2 mg mL<sup>-1</sup>, 0.42, 0.85 and 1.70 mL, respectively) was added dropwise. The obtained suspension was stirred for 30 min at room temperature followed by hydrothermal treatment (HT) at 130 °C for 3 h. The final product, denoted as y%Pd<sub>1+NPs</sub>/CCN<sub>x</sub>, was obtained after water and ethanol washing, successively, followed by being dried at 60 °C. In y%Pd<sub>1+NPs</sub>/CCN<sub>x</sub>, “y%” represented Pd loading level, determined by a Perkin-Elmer Avio 200 ICP-MS.

Bulk g-C<sub>3</sub>N<sub>4</sub> (denoted as CN) was prepared by the similar route to CCN<sub>x</sub> in the absence of uracil, and after hydrothermal treatment of dicyandiamide suspension at 180 °C for 10 h, melamine-cyanuric acid supramolecular aggregate (MCS) was formed. Further calcination of MCS at 550 °C for 3 h at a heating ramp of 3 °C min<sup>-1</sup> under N<sub>2</sub> flow produced CN.

Pd<sub>NPs</sub>/CN was prepared via the same route as that of Pd<sub>1+NPs</sub>/CCN<sub>x</sub> by the replacement of CCN<sub>x</sub> for CN.

Pd<sub>NPs</sub> deposited CCN<sub>3</sub> (denoted to Pd<sub>NPs</sub>/CCN<sub>3</sub>) was prepared by a NaBH<sub>4</sub> reduction reaction according to the literature method [21]. Specifically, CCN<sub>3</sub> (100 mg) was ultrasonically dispersed to water (50 mL) for 30 min, and then PdCl<sub>2</sub> solution (2 mg mL<sup>-1</sup>, 0.42 mL) was added dropwise to the above suspension under stirring. Over period of 1 h, NaBH<sub>4</sub> (0.1 mol L<sup>-1</sup>, 4 mL) was added, and the obtained mixture was continuously stirred for 6 h at room temperature. Finally, the precipitate was centrifuged and then washed with deionized water completely. After being dried at 60 °C for 10 h, the light gray Pd<sub>NPs</sub>/CCN<sub>3</sub> powder was obtained.

Pd<sub>NPs</sub>/CCN<sub>3'</sub> was prepared via the same route as that of Pd<sub>1+NPs</sub>/CCN<sub>3</sub> by the replacement of CCN<sub>3</sub> for CCN<sub>3'</sub>, in which CCN<sub>3'</sub> was prepared by direct thermal copolymerization of dicyandiamide and uracil without supramolecule self-assembly process. Typically, dicyandiamide (10.0 g) and uracil (0.20 g) were thoroughly ground, and the obtained white powder was then calcined at 550 °C for 3 h at a heating ramp of 3 °C min<sup>-1</sup> under N<sub>2</sub> flow to produce CCN<sub>3'</sub>.

### 2.2. Catalyst characterizations

Transmission electron microscope (TEM), high resolution TEM (HRTEM) and the corresponding element mapping images were recorded by a JEM-2100 high resolution transmission electron microscope operating at an accelerating voltage of 200 kV. The high angle annular dark field-scanning transmission electron microscopy (HAADF-STEM) images was taken on a JEOL ARM200CF, fifth order aberration-corrected transmission electron microscopy. Nitrogen gas porosimetry measurement was carried out on a Micrometrics ASAP 2020 M PLUS HD88 surface area and porosity analyzer. The contents of C and N elements in CCN<sub>x</sub> were determined by a EuroVector CHNS EA3000 elemental analyzer. Powder X-ray diffraction (XRD) was measured with a Japan Rigaku D/max 2000 X-ray diffractometer. Fourier transform infrared (FT-IR) spectra were recorded on a Nicolet Magna 560 IR spectrophotometer. Electron spin resonance (ESR) spectra was recorded on a Bruker EMXnano spectrometer (X-band frequency operated at 9.63 GHz with the temperature at 298 K). <sup>13</sup>C cross polarization-magic angle spinning nuclear magnetic resonance (CP-MAS NMR) was recorded on a Bruker AVANCE NEO-600WB spectrometer (600 MHz). X-ray

photoelectron spectroscopy (XPS) was conducted by an Axis Ultra DLD instrument with a monochromated Al-K $\alpha$  source at a residual gas pressure of less than  $10^{-8}$  Pa. Ultraviolet-visible diffuse reflectance spectra (UV-vis/DRS) were recorded on a Cary 500 UV-Vis-NIR spectrometer. Steady-state photoluminescence (PL) emission spectra and time-resolved photoluminescence decay (TRPD) spectra were taken on an FLS-920 fluorescence spectrophotometer (excitation wavelength of 370 nm and emission wavelength of 440 nm). Synchrotron-based X-ray absorption spectroscopy (XAS) including X-ray absorption near edge structure (XANES) and the Fourier transform extended X-ray absorption fine structure (FT-EXAFS) spectroscopy of Pd K-edge were recorded at 21 Å X-ray nanodiffraction beamline of Taiwan Photon Source, National Synchrotron Radiation Research Center. Femtosecond transient absorption (fs-TA) spectroscopy was measured by an automated data acquisition transient absorption spectrometer (Helios Fire, Ultrafast Systems), and amplified femtosecond laser system (OPerA-Solo) combined with a laser system (Coherent Astrella) which was generated about 100 fs pulse at 800 nm with a repetition rate of 1 kHz and an average power of ca. 7.0 mJ. In fs-TA measurements, the white-light continuum probe pulses were focused on the 800 nm beam onto a sapphire plate, which produced probe pulses on the range of 420–780 nm. The time delays (within 8 ns) between the pump and probe pulses were varied by a motorized optical delay line. The instrument response function was determined on 1.4 times of laser pulse time.

### 2.3. Photoelectrochemical measurements

All electrochemical measurements were recorded by a Chenhua CHI 660E electrochemical workstation equipped with a three electrode system. Specifically, L-type glassy carbon coated with the catalyst film on the black round region (diameter of 3.0 mm and area of 7.06 mm<sup>2</sup>) served as the working electrode. Ag/AgCl electrode (saturated KCl) and Pt wire was used as the reference electrode and the counter electrode, respectively. Transient photocurrent (TP) responses were measured in a Na<sub>2</sub>SO<sub>4</sub> solution (0.01 mol L<sup>-1</sup>) and recorded by *i-t* curves with a bias voltage of +1.0 V for 200 s, and simulated sunlight irradiation was provided by Xe lamp (300 W Xe lamp). Electrochemical impedance spectra (EIS) Nyquist plots was recorded in a Na<sub>2</sub>SO<sub>4</sub> solution (0.5 mol L<sup>-1</sup>) with an alternating current voltage amplitude of 5 mV, frequency range of 1000–50 kHz. Mott-Schottky (MS) measurements were performed in Na<sub>2</sub>SO<sub>4</sub> solution (0.5 mol L<sup>-1</sup>) at the potential range of -1.5–0.5 V with an alternating current of 10 mV and recorded by MS plots at three fixed frequencies of 1.3, 1.5 and 2.0 kHz under dark condition.

### 2.4. Photocatalytic hydrogen evolution tests

Photocatalytic H<sub>2</sub> evolution tests were carried out in a top-irradiation quartz reactor, and the reactor connected to a sealed gas circulation system (China Education Au-light). Full solar light spectrum and visible-light irradiation was provided by a CEL-HXE300 Xe lamp (300 W). The catalyst (10 mg) and triethanolamine (TEOA, 5 mL) were added in water (45 mL) followed by dispersing for 5 min at room temperature via sonication, and then the suspension was degassed for 30 min to remove air. The water used for the test had a resistivity of 18 MΩ. The suspension was kept stirring and maintained at 6 °C by cooling water circulation machine (LX-300). The evolved H<sub>2</sub> was sampled every 30 min through an on-line automated flow-injection apparatus and then analyzed by gas chromatography (GC-2014 C, Shimadzu, Japan) with a chromatographic column filled with 5 Å molecular sieve. The operation temperature of GC was 100 °C, and the flow rate of nitrogen gas was 25 mL min<sup>-1</sup>.

Apparent quantum yield (AQY) for H<sub>2</sub> evolution was determined by the similar procedure to the H<sub>2</sub> evolution test, and the irradiation was supplied by a monochromatic light of the Xe lamp equipped with band-pass filter of 365, 400, 450 and 550 nm, respectively. The AQY value was

calculated according to Eq. 1.

$$\text{AQY}(\%) = \frac{2 \times \text{Number of H}_2}{\text{Number of incident photons}} \times 100\% \quad (1)$$

Solar-to-hydrogen (STH) conversion efficiency for H<sub>2</sub> evolution was calculated according to Eq. 2.

$$\text{STH}(\%) = \frac{\text{Energy of generated H}_2}{\text{Energy of the incident solar light}} \times 100\% \quad (2)$$

### 2.5. Theoretical calculations

DFT calculations were performed by using the Vienna Ab initio Simulation Package (VASP), including structural optimization, charge densities, electrostatic potential (ESP), adsorption energy of single Pd atoms and/or Pd nanoparticles, work function and Gibbs free energy. The generalized gradient approximation parametrized was used for the electron exchange-correction function by Perdew-Burke-Ernzerhof (PBE). The k-point mesh of 6 × 6 × 1 was used to perform geometry optimization. The hydrogen absorption free energy ( $\Delta G_{\text{H}^*}$ ) is calculated based on Eq. 3.

$$\Delta G_{\text{H}^*} = \Delta E_{\text{H}^*} + \Delta E_{\text{ZPE}} - T\Delta S_{\text{H}^*} \quad (3)$$

$\Delta E_{\text{H}^*}$  represents the adsorption energy of the H atom.  $\Delta E_{\text{ZPE}}$  is zero-point energy of H atoms in the gas phase. T and  $\Delta S_{\text{H}^*}$  represent the room temperature and entropy change of H<sub>2</sub> under standard conditions, respectively.

## 3. Results and discussion

### 3.1. Preparation and characterization of Pd<sub>1+NP</sub>/CCN<sub>x</sub> heterojunctions

Generally, the sp<sup>2</sup>-hybridized N atoms in “six-fold-cavities” of g-C<sub>3</sub>N<sub>4</sub> possess lone-pair electrons, and they are in favor of the dispersion and immobilization of metal species by the coordination interaction [22,23]. Nevertheless, ionic radius of Pd<sup>2+</sup> (0.85 Å) is relatively small, and the coordination interaction between Pd species and lone pair electrons of sp<sup>2</sup>-hybridized N atom is weak. In fact, the most of Pd species are anchored on bulk g-C<sub>3</sub>N<sub>4</sub> by electrostatic interaction [24], which may impede the formation of single Pd atoms due to the aggregation of Pd species. In order to stabilize single Pd atoms on g-C<sub>3</sub>N<sub>4</sub> framework firmly, the establishment of strong coordination interaction between Pd species and sp<sup>2</sup>-hybridized N atom is essential. To meet this requirement, the introduction of defects in heptazine rings to redistribute the electron density is a promising and effective strategy [25–27]. For this purpose, here foreign C atoms from π-electron-rich small organic molecule, uracil, are doped to heptazine rings by as-designed supramolecule self-assembly of dicyandiamide and uracil followed by thermal polymerization route. Different from the conventional direct thermal copolymerization of small organic molecule with C/N monomer to C atom self-doped g-C<sub>3</sub>N<sub>4</sub> [28,29], as-designed supramolecule self-assembly of dicyandiamide and uracil under hydrothermal environment (180 °C) can avoid the sublimation of dicyandiamide and uracil during subsequent thermal polymerization process. As a result, a definite molecular structure of C atom self-doped g-C<sub>3</sub>N<sub>4</sub> (CCN<sub>x</sub>) is obtained. As illustrated in Fig. 1a, during the hydrothermal treatment process, dicyandiamide undergoes intermolecular cyclization reaction to produce melamine, and part of melamine further hydrolyzes to yield cyanuric acid [30]. Melamine, cyanuric acid and uracil then self-assemble to form hydrogen-bonded melamine-cyanuric acid-uracil supramolecular aggregates (MCUS, confirmed by XRD, Fig. S1); meanwhile, by using this oxygen containing-MCUS aggregate as the starting materials for the preparation of g-C<sub>3</sub>N<sub>4</sub>, the thermal polymerization process is stimulated. Correspondingly, a definite molecular structure of C atom self-doped g-C<sub>3</sub>N<sub>4</sub> (CCN<sub>x</sub>) is obtained. In comparison of the six-membered ring structure of melamine or cyanuric acid molecule, the

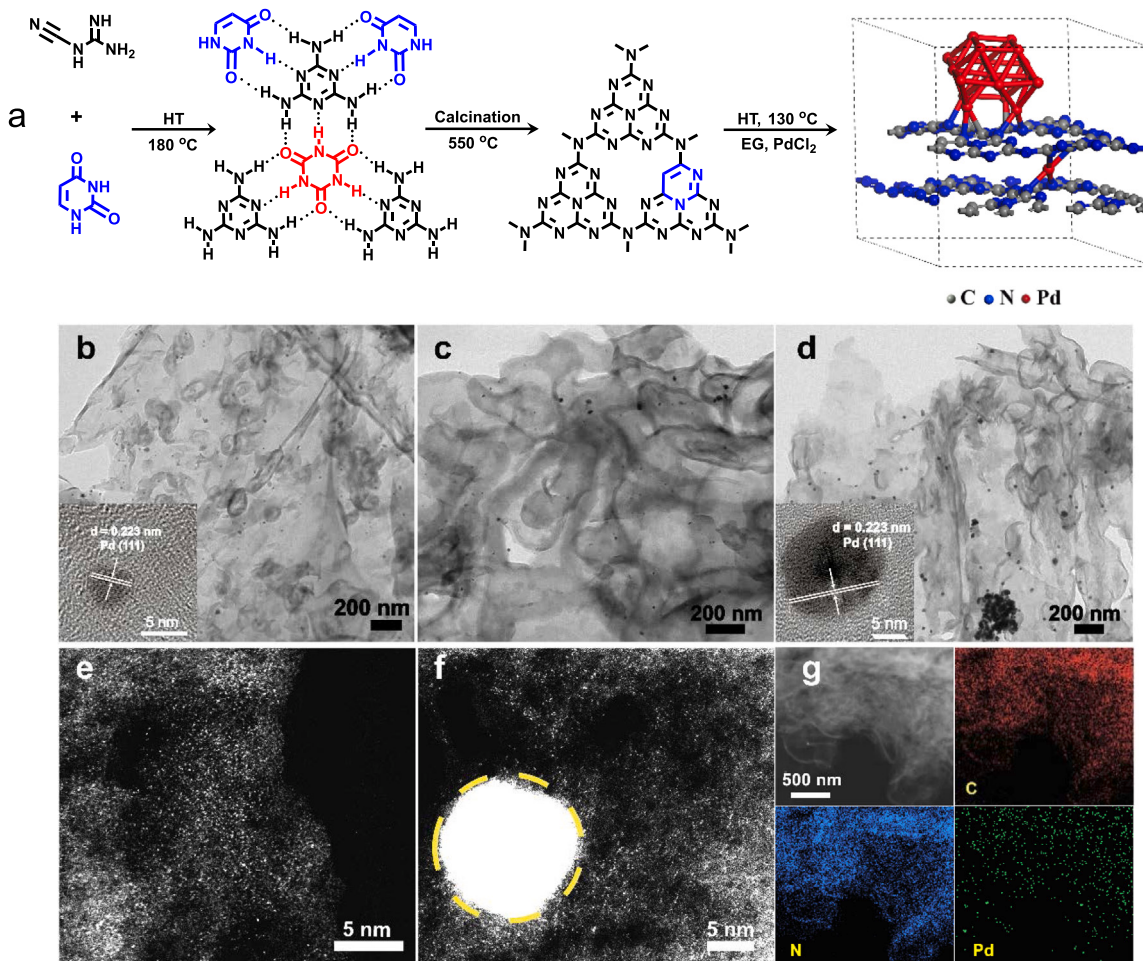


**Fig. 1.** Schematic illustration of the preparation route and framework structure of Pd<sub>1+NPs</sub>/CCN<sub>x</sub> (a). TEM images of 0.33%Pd<sub>1+NPs</sub>/CCN<sub>3</sub> (b), 0.51%Pd<sub>1+NPs</sub>/CCN<sub>3</sub> (c) and 0.97%Pd<sub>1+NPs</sub>/CCN<sub>3</sub> (d). HAADF-STEM images of 0.33%Pd<sub>1+NPs</sub>/CCN<sub>3</sub> (e) and 0.97%Pd<sub>1+NPs</sub>/CCN<sub>3</sub> (f). TEM-elemental mapping images of 0.33%Pd<sub>1+NPs</sub>/CCN<sub>3</sub> (g).

ring structure of uracil molecule has one more C atom but one less N atom, therefore, some C<sub>4</sub>N<sub>2</sub> units from uracil are incorporated to heptazine rings of g-C<sub>3</sub>N<sub>4</sub> during the thermal polymerization process (see <sup>13</sup>C CP-MAS NMR spectra, Fig. 2d). Additionally, by adjusting uracil-to-dicyandiamide molar ratio in the preparation system, C doping level in CCNx is controlled precisely and thus the adjustable electronic structure and band structure. Since N atom is highly electronegative with respect to C atom, C<sub>4</sub>N<sub>2</sub> unit as an electron donor can transfer electron to triazine ring (an electron acceptor), which finally leads to the increased electron density around sp<sup>2</sup>-hybridized N atom in CCNx framework. Thus, an exciting opportunity to strongly coordinate N atoms with Pd atoms is created, which is the most important factor for tightly anchoring and homogeneously dispersing single Pd atoms on CCNx. After low-temperature (130 °C) hydrothermal treatment of CCNx and PdCl<sub>2</sub> in EG system, Pd<sub>1</sub> and small Pd<sub>NPs</sub> co-anchored CCNx heterojunctions (Pd<sub>1+NPs</sub>/CCN<sub>x</sub>) are facilely obtained.

To reveal the morphology and coordination environment of Pd<sub>1</sub> and Pd<sub>NPs</sub> in Pd<sub>1+NPs</sub>/CCN<sub>x</sub> heterojunctions, following powerful characterization technique combined with DFT calculations are conducted. Firstly, simultaneous dispersion of isolated Pd<sub>1</sub> atoms and the deposition of small Pd<sub>NPs</sub> on CCNx are observed visually by TEM and HAADF-STEM techniques, and 0.33%Pd<sub>1+NPs</sub>/CCN<sub>3</sub>, 0.51%Pd<sub>1+NPs</sub>/CCN<sub>3</sub> and 0.97%Pd<sub>1+NPs</sub>/CCN<sub>3</sub> are chosen as the representative samples. TEM images presented in Fig. 1b–d indicate that the samples show layer-stacking wrinkle sheet-like nanostructures, and some unevenly distributed pores are found on the nanosheets; additionally, certain small

nanostructures are deposited on the nanosheets homogeneously. HRTEM images show that the fringe spacing of the nanoparticle is 0.223 nm (insets of Fig. 1b and d), which corresponds to (111) lattice plane of face-centered cubic Pd [18]. Therefore, Pd<sub>1+NPs</sub>/CCN<sub>3</sub> heterojunctions have some Pd<sub>NPs</sub>, and the average particle size of Pd<sub>NPs</sub> increases from 3 (Fig. 1b) to 10 nm (Fig. 1d) as the increment of Pd loading level from 0.33 to 0.97%, reflecting the increased agglomeration of Pd nanoparticles with higher Pd loading level. HAADF-STEM images of 0.33%Pd<sub>1+NPs</sub>/CCN<sub>3</sub> and 0.97%Pd<sub>1+NPs</sub>/CCN<sub>3</sub> provide a direct evidence to confirm the presence of atomically dispersed Pd on CCN<sub>3</sub> (Fig. 1e and f), indicated by the appearance of individual and well-distributed bright spots with the average particle size of ca. 0.2 nm. Additionally, certain small Pd nanoparticles with size of ca. 10 nm are also visibly observed in 0.97%Pd<sub>1+NPs</sub>/CCN<sub>3</sub> heterojunctions, consistent with TEM measurement. TEM-elemental mapping images of 0.33%Pd<sub>1+NPs</sub>/CCN<sub>3</sub> show that C, N and Pd elements are homogeneously dispersed throughout CCN<sub>3</sub> support (Fig. 1g).

The generation of small Pd nanoparticles in Pd<sub>1+NPs</sub>/CCN<sub>x</sub> heterojunctions is due to the introduction of high loading level of Pd species, and certain Pd species aggregate to small Pd nanoparticles. To further confirm this speculation, 0.21%Pd<sub>1+NPs</sub>/CCN<sub>3</sub> and 1.98%Pd<sub>1+NPs</sub>/CCN<sub>3</sub> heterojunctions with lower and higher Pd loading level are prepared, respectively. HAADF-STEM analysis reveals that Pd species in 0.21%Pd<sub>1+NPs</sub>/CCN<sub>3</sub> are mainly pure single atoms (Fig. S2a), while single Pd atoms and larger Pd nanoparticles (average particle size of ca. 15 nm) co-exist in 1.98%Pd<sub>1+NPs</sub>/CCN<sub>3</sub> (Fig. S2b).

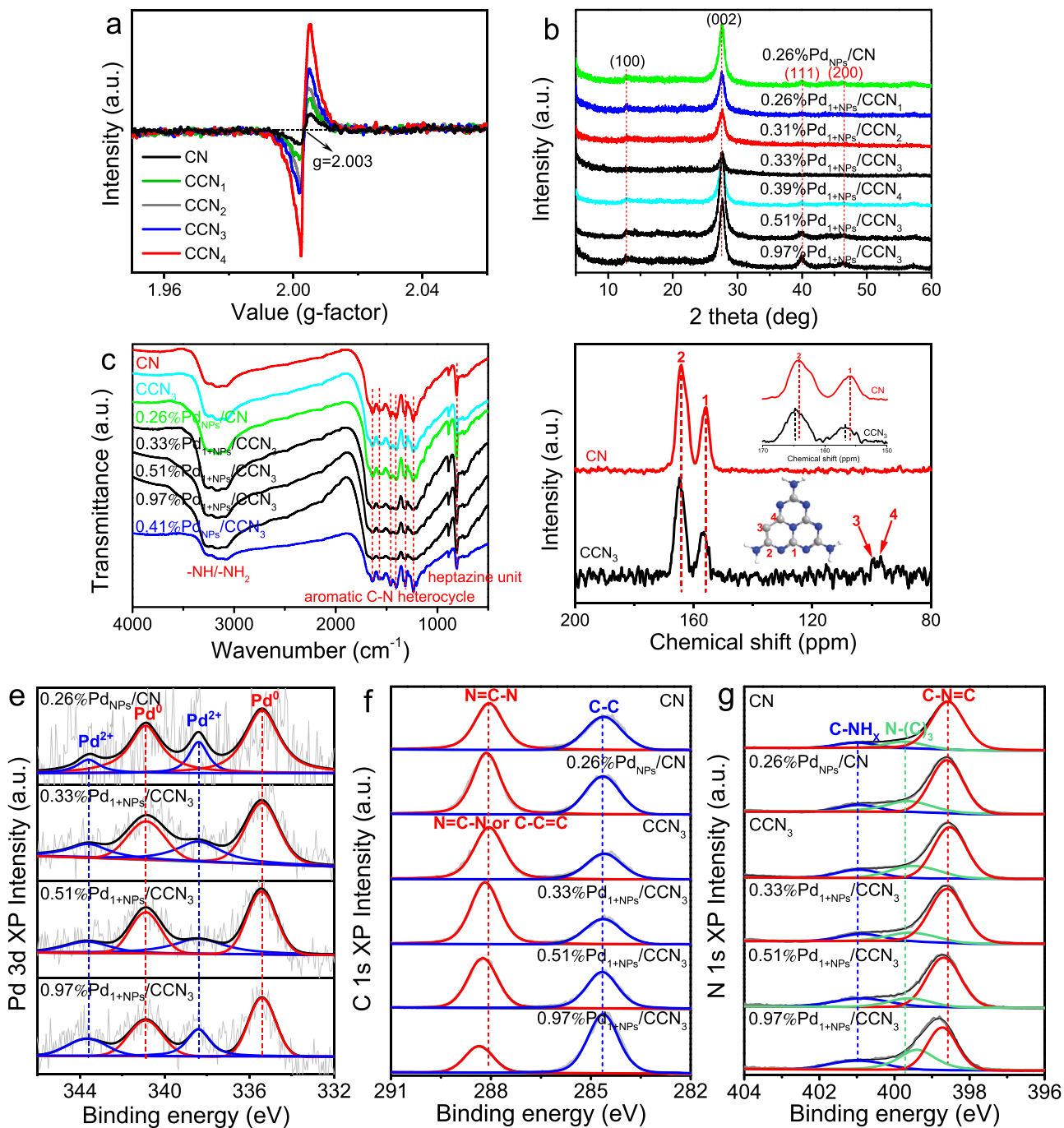


**Fig. 2.** Structural characterization of CCNx and Pd<sub>1+NPs</sub>/CCNx heterojunctions. ESR spectra (a), XRD patterns (b), FT-IR spectra (c), <sup>13</sup>C CP-MAS NMR spectra (d) and high resolution XPS spectra in the Pd 3d (e), C 1 s (f) and N 1 s (g) binding energy regions.

For the reference catalysts including 0.26%Pd<sub>NPs</sub>/CN, 0.41%Pd<sub>NPs</sub>/CCN<sub>3</sub> and 0.34%Pd<sub>NPs</sub>/CCN<sub>3</sub>' prepared at the same theoretical Pd loading level (0.5%) with that of 0.33%Pd<sub>1+NPs</sub>/CCN<sub>3</sub> but different g-C<sub>3</sub>N<sub>4</sub> supports or Pd species deposition method, larger Pd nanoparticles are visibly observed from their TEM images (Fig. S4a—c); moreover, obvious agglomeration of Pd nanoparticles is found in both 0.41%Pd<sub>NPs</sub>/CCN<sub>3</sub> (Fig. S4b) and 0.34%Pd<sub>NPs</sub>/CCN<sub>3</sub>' (Fig. S4c) samples. To further prove the absence of single Pd atoms in 0.26%Pd<sub>NPs</sub>/CN heterojunction, HAADF-STEM observation is carried out. From low-resolution HAADF-STEM image of 0.26%Pd<sub>NPs</sub>/CN it can clearly observe Pd nanoparticles with the average particle size of ca. 14 nm in the sample (Fig. S3a), while no any individual bright spot that corresponds to single Pd atom is found in the high-resolution HAADF-STEM image (Fig. S3b). The result

is originated from weak coordination interaction between Pd species and lone pair electrons of sp<sup>2</sup>-hybridized N atom in “six-fold-cavities” of bulk g-C<sub>3</sub>N<sub>4</sub> and thus the agglomeration of Pd species to nanoparticles.

The contents of C and N elements in four CCNx supports are determined by a CHN elemental analysis method, and then C-to-N molar ratios are calculated. As listed in Table S5, gradually increased C-to-N molar ratio from CN (0.654), CCN<sub>1</sub> (0.660), CCN<sub>2</sub> (0.666), CCN<sub>3</sub> (0.673) to CCN<sub>4</sub> (0.688) is in line with the elevated C element content in CCNx with the increment of uracil-to-dicyandiamide molar ratio from 0, 0.005, 0.0075, 0.015 to 0.030. Nitrogen gas porosimetry measurement shows that the BET surface area (36.7–43.3 m<sup>2</sup> g<sup>-1</sup>) and pore volume (0.26–0.34 cm<sup>3</sup> g<sup>-1</sup>) of CCNx increase gradually as increasing uracil-to-dicyandiamide molar ratio, and the values are higher than CN (32.5 m<sup>2</sup>

$\text{g}^{-1}$  and  $0.22 \text{ cm}^3 \text{ g}^{-1}$ , Fig. S5 and Table S1). The results are originated from the etching of  $\text{g-C}_3\text{N}_4$  nanosheets by the escaped gases such as  $\text{CO}_2$ ,  $\text{H}_2\text{O}$  and  $\text{NH}_3$  during MCS or MCUS thermal polymerization process, which results in the generation of some pores on the nanosheets and thus the ameliorated porosity properties. After the introduction of Pd species, for example,  $0.33\%\text{Pd}_{1+\text{NPs}}/\text{CCN}_3$  sample, changes of its BET surface area ( $45.0 \text{ m}^2 \text{ g}^{-1}$ ) and pore volume ( $0.31 \text{ cm}^3 \text{ g}^{-1}$ ) are limited.

ESR spectra can identify the spin state of unpaired and/or delocalized electrons directly in  $\text{CCN}_x$  structure, which is applied to study the structural defects of  $\text{CCN}_x$  due to C atom self-doping modification. As displayed in Fig. 2a, the signal of Lorentzian line emerges at  $g$  value of 2.003 for CN and each  $\text{CCN}_x$  sample, contributing from unpaired and/or delocalized electrons in  $\text{g-C}_3\text{N}_4$  structure [31]. For CN, the intensity of Lorentzian line is absolutely weak because only a few unpaired electrons exist in the edges of the heptazine rings due to uncompleted thermal polymerization of MCS. However, a noticeably enhanced intensity of the ESR signal is found in  $\text{CCN}_x$  samples, and the intensity increases continuously with the increment of C doping level. The result indicates an increased concentration of the delocalized electrons in the  $\pi$ -conjugated aromatic C–N heterocycles of  $\text{CCN}_x$  due to C atom self-doping. As-generated more delocalized electrons correspond to more abundant defective sites. Therefore, the concentrations of C atom self-doped-induced defects are controllable by adjusting uracil-to-dicyandiamide molar ratio in  $\text{CCN}_x$  preparation system.

XRD patterns of CN and  $\text{CCN}_x$  all demonstrate the characteristic peaks at  $27.6^\circ$  (002) and  $12.9^\circ$  (100) (Fig. S1b), which are assigned to the  $\pi$ - $\pi$  interlayer stacking of aromatic C–N heterocycles and the in-plane repetitive heptazine rings, respectively [32]. The result suggests that the conjugated aromatic C–N heterocycles still maintain periodic stacking after C atom self-doping; nonetheless, the intensity of (002) diffraction peak of  $\text{CCN}_4$  decreases obviously, indicating that higher C doping level may decrease the periodicity of layered  $\text{g-C}_3\text{N}_4$  structure, caused by as-formed structural defects. After the introduction of Pd species with lower and similar loading level (0.26–0.39%) to different  $\text{CCN}_x$  supports, the above two characteristic peaks are still visibly found, reflecting the retention of the layered structure of  $\text{g-C}_3\text{N}_4$ ; additionally, no corresponding signals associated with crystalline Pd NPs are identified (Fig. 2b). As increasing Pd doping level to 0.51% and 0.97% on  $\text{CCN}_3$  support, two weak peaks at  $40.1^\circ$  and  $46.6^\circ$  emerge, and they are attributed to (111) and (200) facets of metallic  $\text{Pd}^0$  [33]. The result firmly evidences the presence of some  $\text{Pd}_{\text{NPs}}$  in  $\text{Pd}_{1+\text{NPs}}/\text{CCN}_x$  heterojunctions at higher Pd loading level. As for  $0.26\%\text{Pd}_{\text{NPs}}/\text{CN}$ , the weak peaks at  $40.1^\circ$  and  $46.6^\circ$  are also detected although lower Pd loading level, similar results are also found in  $0.41\%\text{Pd}_{\text{NPs}}/\text{CCN}_3$  and  $0.34\%\text{Pd}_{\text{NPs}}/\text{CCN}_3$  samples (Fig. S1c). Therefore, Pd species existing in three reference catalysts are mainly in the form of Pd nanoparticles.

FT-IR spectra can provide interesting structural information related to the interactions between  $\text{Pd}_1$  and  $\text{CCN}_x$  framework except for the primary molecular structure of  $\text{g-C}_3\text{N}_4$ . As shown in Fig. 2c, the appearance of a series of characteristic vibrational peaks at 816 (breathing vibration of heptazine units), 1200–1700 (stretching vibrations of aromatic C–N heterocycles) and  $2800\text{--}3500^{-1}$  (stretching vibrations of terminal  $-\text{NH}/\text{NH}_2$  groups) in  $\text{CCN}_3$ ,  $\text{Pd}_{1+\text{NPs}}/\text{CCN}_3$  (including  $0.33\%\text{Pd}_{1+\text{NPs}}/\text{CCN}_3$ ,  $0.51\%\text{Pd}_{1+\text{NPs}}/\text{CCN}_3$  and  $0.97\%\text{Pd}_{1+\text{NPs}}/\text{CCN}_3$ ),  $0.26\%\text{Pd}_{\text{NPs}}/\text{CN}$  and  $0.41\%\text{Pd}_{\text{NPs}}/\text{CCN}_3$  samples implies that the primary molecular structure of  $\text{g-C}_3\text{N}_4$  is remained after C atom self-doping and/or the introduction of Pd species [34,35]. Additionally, for three  $\text{Pd}_{1+\text{NPs}}/\text{CCN}_3$  heterojunctions, the vibrational peak intensities of aromatic C–N heterocycles become weak in comparison of  $\text{CCN}_3$  support; moreover, as increasing Pd loading level from 0.33 to 0.97%, the peak intensity decreases gradually. This phenomenon is not observed in the reference catalysts such as  $0.26\%\text{Pd}_{\text{NPs}}/\text{CN}$  and  $0.41\%\text{Pd}_{\text{NPs}}/\text{CCN}_3$ , highlighting the strong chemical interactions between single Pd atoms (rather than Pd nanoparticles) and  $\text{sp}^2$ -hybridized N atom of  $\text{CCN}_3$ . The detailed characterization of this interaction is carried out by subsequent  $^{13}\text{C}$  CP-MAS NMR, XPS and synchrotron-based XAS

measurements.

Small amount of C atom self-doped within heptazine structure of  $\text{g-C}_3\text{N}_4$  causes a slightly altered chemical environment of C1 atoms from  $\text{N}=\text{C}-\text{N}_2$  and C2 atoms from  $\text{N}=\text{C}-\text{N}(\text{NH}_x)$  as well as the generation of a couple of new C species, i.e., C3 atoms from  $\text{C}=\text{C}-\text{C}$  and C4 atoms from  $\text{C}-\text{C}=\text{N}$ , which clearly reflects in the  $^{13}\text{C}$  CP-MAS NMR spectrum of  $\text{CCN}_3$ . As shown in Fig. 2d, in comparison of  $^{13}\text{C}$  CP-MAS NMR spectrum of CN with the characteristic signals at 155.9 (C1) and 164.1 ppm (C2) [28], the signals of  $\text{CCN}_3$  shift to higher chemical shift values, i.e., 156.9 (C1) and 164.7 ppm (C2) (inset in Fig. 2d). The result indicates somewhat decreased electron density around C1 and C2 atoms in C atom-self-doped heptazine units because some electrons in C atom-self-doped triazine rings donate to the neighboring triazine rings. In addition, two weak signals emerge at 99.5 (C3) and 96.9 (C4) ppm, which correspond to aromatic  $\text{C}=\text{C}-\text{C}$  and  $\text{C}-\text{C}=\text{N}$  units in heptazine structure of  $\text{CCN}_x$  [36–38]. Combination of the literature work [20], as-designed supramolecule self-assembly of dicyandiamide and uracil followed by thermal polymerization route as well as the specific structure of  $\pi$ -electron-rich uracil molecules it is reasonably speculated that  $\text{C}_4\text{N}_2$  units are incorporated to the heptazine units to form C atom-self doped  $\text{g-C}_3\text{N}_4$ .

The surface chemical states of Pd, C and N elements in three  $\text{Pd}_{1+\text{NPs}}/\text{CCN}_3$  heterojunctions are studied by a XPS surface probe technique. From Pd 3d high resolution XPS of three  $\text{Pd}_{1+\text{NPs}}/\text{CCN}_3$  heterojunctions shown in Fig. 2e it is found that both metallic  $\text{Pd}^0$  and  $\text{Pd}^{2+}$  species are identified with binding energy (BE) of 335.3 ( $\text{Pd } 3\text{d}_{5/2}$ ) and 340.8 eV ( $\text{Pd } 3\text{d}_{3/2}$ ) as well as 338.3 ( $\text{Pd } 3\text{d}_{5/2}$ ) and 343.6 eV ( $\text{Pd } 3\text{d}_{3/2}$ ), respectively [39,40]. Similar result is also obtained in  $0.26\%\text{Pd}_{\text{NPs}}/\text{CN}$  heterojunction. Furthermore, for three  $\text{Pd}_{1+\text{NPs}}/\text{CCN}_3$  heterojunctions,  $\text{Pd}^0$ -to- $\text{Pd}^{2+}$  peak area ratio increases gradually from 1.69, 1.72 to 1.80 with the increment of Pd loading level from 0.33, 0.51 to 0.97%, suggesting slightly increased number of Pd nanoparticles in the heterojunctions. In the case of  $0.26\%\text{Pd}_{\text{NPs}}/\text{CN}$ , its  $\text{Pd}^0$ -to- $\text{Pd}^{2+}$  peak area ratio reaches up to 4.03, much higher than that of its  $0.33\%\text{Pd}_{1+\text{NPs}}/\text{CCN}_3$  counterpart, which further evidences that  $\text{Pd}_{\text{NPs}}$  are predominant in bulk CN-immobilized Pd species.

In the C 1 s high resolution XPS of CN (Fig. 2f), two peaks centering at 288.1 and 284.6 eV are identified, and they are assigned to the  $\text{N}=\text{C}-\text{N}$  coordinations in the repetitive heptazine rings and  $\text{C}=\text{C}$  bonds in reference substance, respectively [41]. In the case of  $\text{CCN}_3$ , the above characteristic peaks are still identified without the shift of the BE values, and it should be noted that the peak at 288.1 eV is originated from the contribution of both  $\text{N}=\text{C}-\text{N}$  and  $\text{C}=\text{C}=\text{C}$  coordinations. Interestingly, after the introduction of Pd species to  $\text{CCN}_3$  support, the  $\text{N}=\text{C}-\text{N}$  coordinations shift to a high BE region, and continuous shift of  $\text{N}=\text{C}-\text{N}$  peak to higher BE region occurs as increasing Pd loading level, namely, 288.2, 288.3 and 288.5 eV for  $0.33\%\text{Pd}_{1+\text{NPs}}/\text{CCN}_3$ , 0.51%  $\text{Pd}_{1+\text{NPs}}/\text{CCN}_3$  and 0.97%  $\text{Pd}_{1+\text{NPs}}/\text{CCN}_3$ , respectively. The result indicates somewhat decrease of electron density in  $\text{N}=\text{C}=\text{N}$  coordinations. This electron density redistribution is caused by as-formed Pd–N coordination bonding in  $\text{Pd}_{1+\text{NPs}}/\text{CCN}_3$ , and electrons from  $\text{sp}^2$ -hybridized N atoms donate to Pd atoms. Nevertheless, the shift of BE value of  $\text{N}=\text{C}=\text{N}$  peak in  $0.26\%\text{Pd}_{\text{NPs}}/\text{CN}$  is neglectable, which indirectly verifies that the weak Pd–N coordination interaction or electrostatic interaction exists between  $\text{sp}^2$ -hybridized N atoms in bulk CN with Pd atoms.

Fig. 2g displays N 1 s high resolution XPS of CN,  $\text{CCN}_3$ ,  $\text{Pd}_{\text{NPs}}/\text{CN}$  and  $\text{Pd}_{1+\text{NPs}}/\text{CCN}_3$  samples. It shows that three peaks centering at 398.5, 399.7 and 401.0 eV are emerged in CN, and they are assigned to two-coordinated nitrogen ( $\text{C}=\text{N}=\text{C}$  or  $\text{N}_{2\text{C}}$ ), three-coordinated nitrogen ( $\text{N}-(\text{C})_3$  or  $\text{N}_{3\text{C}}$ ) and N atoms from unpolymerized  $-\text{NH}/-\text{NH}_2$  group, respectively [42]. After C atom self-doping, these characteristic BE peaks still are detected, and the shifts of the peaks are hardly observed. However, obvious and continuous shift of  $\text{N}_{2\text{C}}$  peak to high BE value occurs for  $0.33\%\text{Pd}_{1+\text{NPs}}/\text{CCN}_3$  (398.6 eV), 0.51%  $\text{Pd}_{1+\text{NPs}}/\text{CCN}_3$  (398.7 eV) and 0.97%  $\text{Pd}_{1+\text{NPs}}/\text{CCN}_3$  (398.8 eV), suggesting gradually

decreased electron density in C–N=C coordinations. For 0.26% Pd<sub>NPs</sub>/CN, the shift of N<sub>2C</sub> peak is undetectable. The result further proves the strong coordination ability of sp<sup>2</sup>-hybridized N atoms in CCN<sub>3</sub> with Pd atoms, and thereby single Pd atoms are firmly stabilized on CCN<sub>3</sub> by the formation of strong Pd–N coordination bonds.

Next, to gain a deep and comprehensive understanding on the chemical state and coordination environment of Pd species in Pd<sub>1+NPs</sub>/CCN<sub>x</sub> heterojunctions, the powerful synchrotron-based XAS technique is applied, and the 0.33%Pd<sub>1+NPs</sub>/CCN<sub>3</sub> is chosen as a representative sample (Fig. 3). As shown in Fig. 3a, detailed information of Pd oxidation states in 0.33%Pd<sub>1+NPs</sub>/CCN<sub>3</sub> is provided by Pd K-edge XANES spectra. It shows that the absorption edge position of 0.33%Pd<sub>1+NPs</sub>/CCN<sub>3</sub> is between that of Pd foil and PdO; additionally, the absorption edge of 0.33%Pd<sub>1+NPs</sub>/CCN<sub>3</sub> is closer to Pd foil. Therefore, some positively charged Pd<sup>δ+</sup> and metallic Pd<sup>0</sup> species are both formed in 0.33% Pd<sub>1+NPs</sub>/CCN<sub>3</sub> heterojunction. Information regarding to the local coordination environment of Pd species in 0.33%Pd<sub>1+NPs</sub>/CCN<sub>3</sub> is obtained from Pd K-edge FT-EXAFS analysis (Fig. 3b), and the peaks identified at 1.5 and 2.6 Å corresponds to Pd–N and Pd–Pd coordinations, respectively, in contrast with those of reference PdO and Pd foil [43]. Therefore, it is strongly suggested that atomically dispersed Pd<sub>1</sub> and Pd<sub>NPs</sub> co-anchored on CCN<sub>3</sub> in Pd<sub>1+NPs</sub>/CCN<sub>3</sub> heterojunction, which coincides with HAADF-STEM measurement.

To determine the quantitative structure parameters of Pd<sub>1</sub> and Pd<sub>NPs</sub> in 0.33%Pd<sub>1+NPs</sub>/CCN<sub>3</sub>, Pd K-edge FT-EXAFS fitting curves at R space (Fig. 3c and Fig. S6) and k space (Fig. S7) are provided, and the fitting parameters are summarized in Table S2. According to the fitting results, the estimated coordination number of Pd–Pd in 0.33%Pd<sub>1+NPs</sub>/CCN<sub>3</sub> is 7; simultaneously, one Pd<sub>1</sub> coordinates with four N atoms to form Pd–N<sub>4</sub> configuration in 0.33%Pd<sub>1+NPs</sub>/CCN<sub>3</sub>.

Morlet wavelet transformation (WT) analysis of the Pd K-edge EXAFS

oscillation further confirms the coexistence of Pd single atoms and nanoparticles in 0.33%Pd<sub>1+NPs</sub>/CCN<sub>3</sub> heterojunction. Specifically, WT analysis of Pd foil shows only one Pd–Pd peak at R = 2.6 Å and k = 9.6 Å<sup>-1</sup> (Fig. 3d), while PdO has two main peaks at R = 1.6 Å and k = 5.1 Å<sup>-1</sup> (Pd–O) as well as R = 3.0 Å and k = 8.8 Å<sup>-1</sup> (Pd–Pd) coordinations, respectively (Fig. 3e). In the case of 0.33%Pd<sub>1+NPs</sub>/CCN<sub>3</sub>, two peaks located at R = 1.5 Å and k = 3.0 Å<sup>-1</sup> as well as R = 2.6 Å and k = 7.1 Å<sup>-1</sup> emerge, and they are attributed to Pd–N and Pd–Pd scattering, respectively (Fig. 3f).

On the basis of the above structural characterization results, the possible coordination approaches of Pd species on CN and CCN<sub>x</sub> supports are proposed, and the corresponding adsorption energy ( $E_{ads}$ ) values of Pd<sub>1</sub> and Pd<sub>NPs</sub> at different anchoring sites are calculated. As shown in Fig. 4a, in CN immobilized Pd species, Pd atoms are confined in “six-fold-cavities” by weak coordination or electrostatic interaction with N atoms because ionic radius of Pd<sup>2+</sup> is relatively small, and the orbital overlap between Pd atoms and sp<sup>2</sup>-hybridized N atoms in CN is weak. The assumption is consistent with the calculated  $E_{ads}$  value (-2.07 eV). As for CCN<sub>x</sub> immobilized Pd species, if Pd atoms locate in in-plane “six-fold-cavities” of CCN<sub>x</sub>, Pd–N<sub>2</sub> coordination configuration is preferable because of the enlarged electron density around sp<sup>2</sup>-hybridized N atoms in CCN<sub>x</sub> structure (Fig. 4b). The speculation is evidenced by the notably increased  $E_{ads}$  value (-3.05 eV). However, according to Pd K-edge FT-EXAFS analysis, the coordination number of Pd–N is 4, and thus another coordination approach, interlayer four-coordinated Pd–N bonds, are supposed to be established for stabilizing single Pd atoms in CCN<sub>x</sub> framework. The speculation is reasonable because the calculated  $E_{ads}$  value is extremely high (-4.21 eV, Fig. 4d), much higher than that of interlayer four-coordinated Pd–N bonds formed in CN framework (-2.81 eV, Fig. 4c). The result further verifies the importance of C atom self-doping for regulating the electron structure of g-C<sub>3</sub>N<sub>4</sub> and thereby

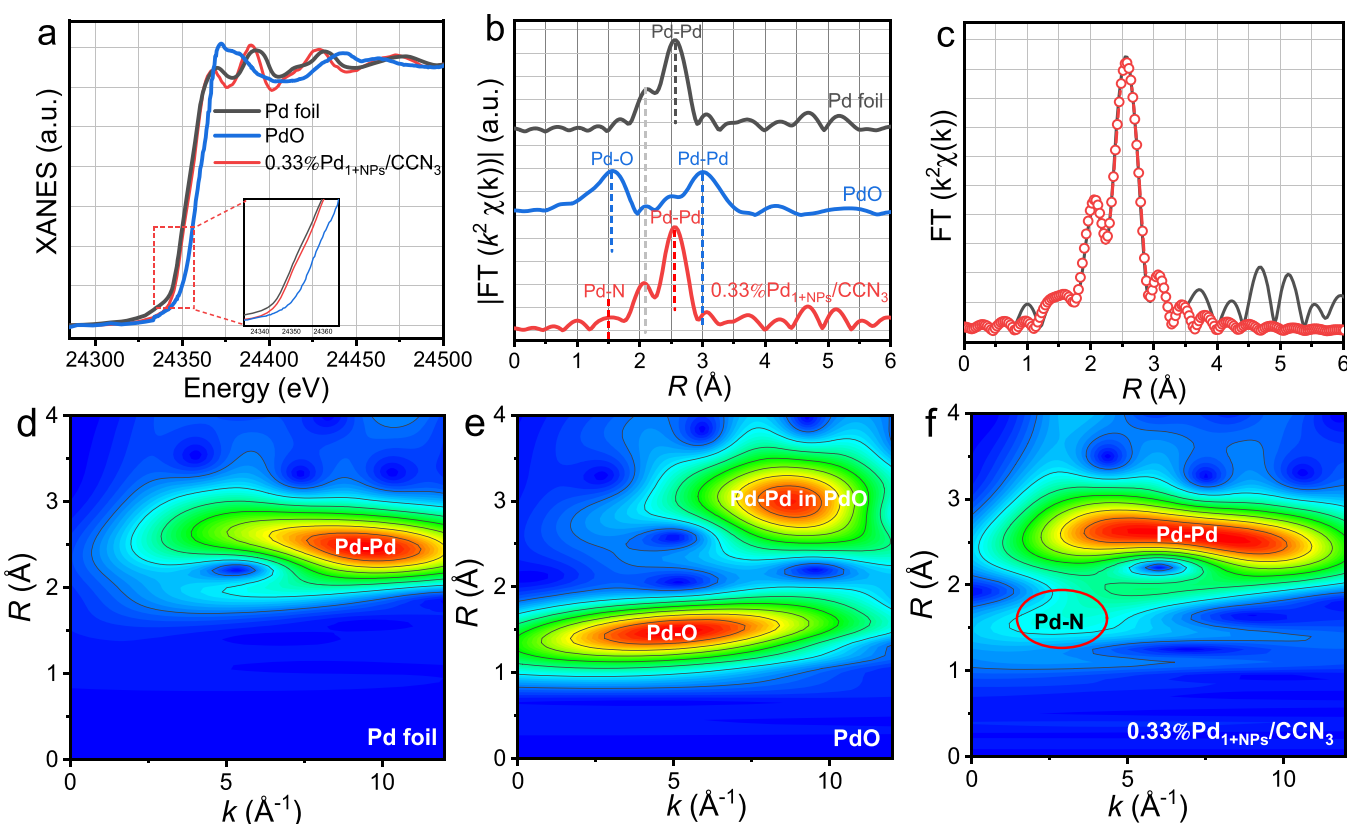


**Fig. 3.** Normalized Pd K-edge XANES spectra (a) and  $k^2$ -weighted Pd K-edge FT-EXAFS spectra at R space (b) of 0.33%Pd<sub>1+NPs</sub>/CCN<sub>3</sub> heterojunction and reference Pd foil and PdO samples. The  $k^2$ -weighted Pd K-edge EXAFS experimental data and fitting curve of 0.33%Pd<sub>1+NPs</sub>/CCN<sub>3</sub> heterojunction at R space (c). Wavelet transform of Pd foil (d), PdO (e) and 0.33%Pd<sub>1+NPs</sub>/CCN<sub>3</sub> (f).

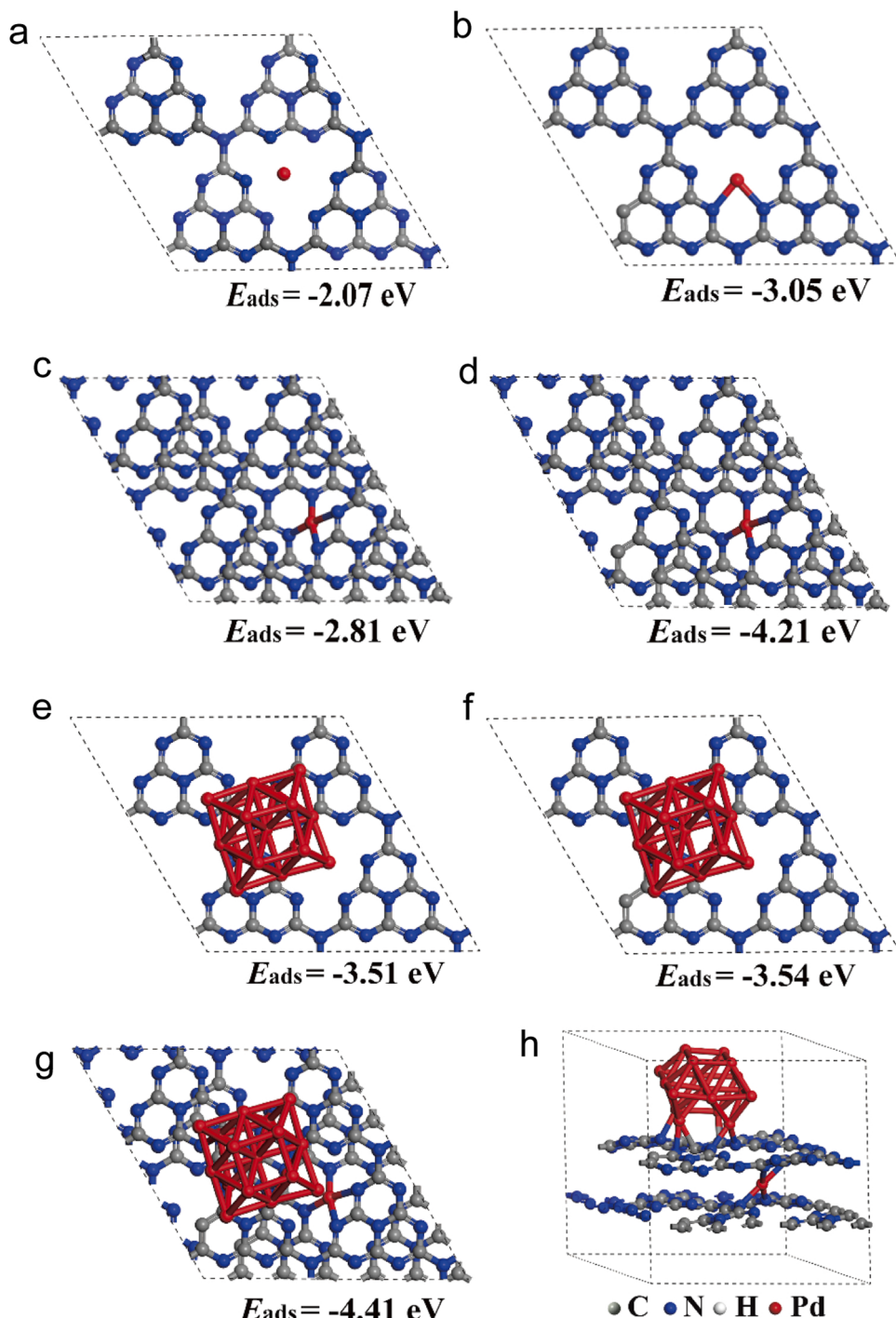


**Fig. 4.** The possible coordination approaches of  $\text{Pd}_1$  (a–d) and  $\text{Pd}_{\text{NPs}}$  (e, f) on CN and  $\text{CCN}_x$  supports and the corresponding  $E_{\text{ads}}$  values of  $\text{Pd}_1$  and  $\text{Pd}_{\text{NPs}}$  at different anchoring sites. The proposed coordination approaches of both  $\text{Pd}_1$  and  $\text{Pd}_{\text{NPs}}$  on  $\text{CCN}_x$  support (g: top view; h: side view) and the corresponding  $E_{\text{ads}}$  values.

the coordination environment of Pd atoms. In the cases of CN and  $\text{CCN}_x$  immobilized  $\text{Pd}_{\text{NPs}}$ ,  $\text{Pd}_{\text{NPs}}$  prefer to deposit on the in-plane heptazine rings due to larger particle size, and the calculated  $E_{\text{ads}}$  values of  $\text{Pd}_{\text{NPs}}$  on CN ( $-3.51$  eV, Fig. 4e) and  $\text{CCN}_x$  ( $-3.54$  eV, Fig. 4f) are the same and large enough. The result suggests that the change of electron structure of  $\text{g-C}_3\text{N}_4$  has little influence on the deposition of  $\text{Pd}_{\text{NPs}}$ . Based on the above discussion, the most energetic coordination configuration of co-anchored  $\text{Pd}_1$  and  $\text{Pd}_{\text{NPs}}$  on  $\text{CCN}_x$  support is proposed and illustrated in Fig. 4g and h (top and side view). Specifically, interlayer  $\text{Pd}-\text{N}_4$  coordination is the most stable configuration, and it is favorable for effective spatial isolation of Pd species at the atomic level to generate

positively charged single Pd atoms; simultaneously, other Pd species agglomerate to form small  $\text{Pd}_{\text{NPs}}$  that locate on the in-plane heptazine rings. It should be noted that Pd atom in its ground state shows a  $4d^{10}$  electron configuration. Nevertheless, when Pd atom is in the ligand field of  $\text{sp}^2$ -hybridized N atoms of  $\text{g-C}_3\text{N}_4$ , its d orbital energy level splitting happens due to the perturbation of the N atoms, and therefore Pd  $4d^85s^2$  electron configuration is preferable, which favors a  $\text{Pd}-\text{N}_4$  square planar coordination geometry in  $\text{Pd}_{1+\text{NPs}}/\text{CCN}_x$  to stabilize single Pd atoms.

Change of electronic structure of  $\text{g-C}_3\text{N}_4$  owing to C atom self-doping modification is also reflected in their UV-vis/DRS. As displayed in

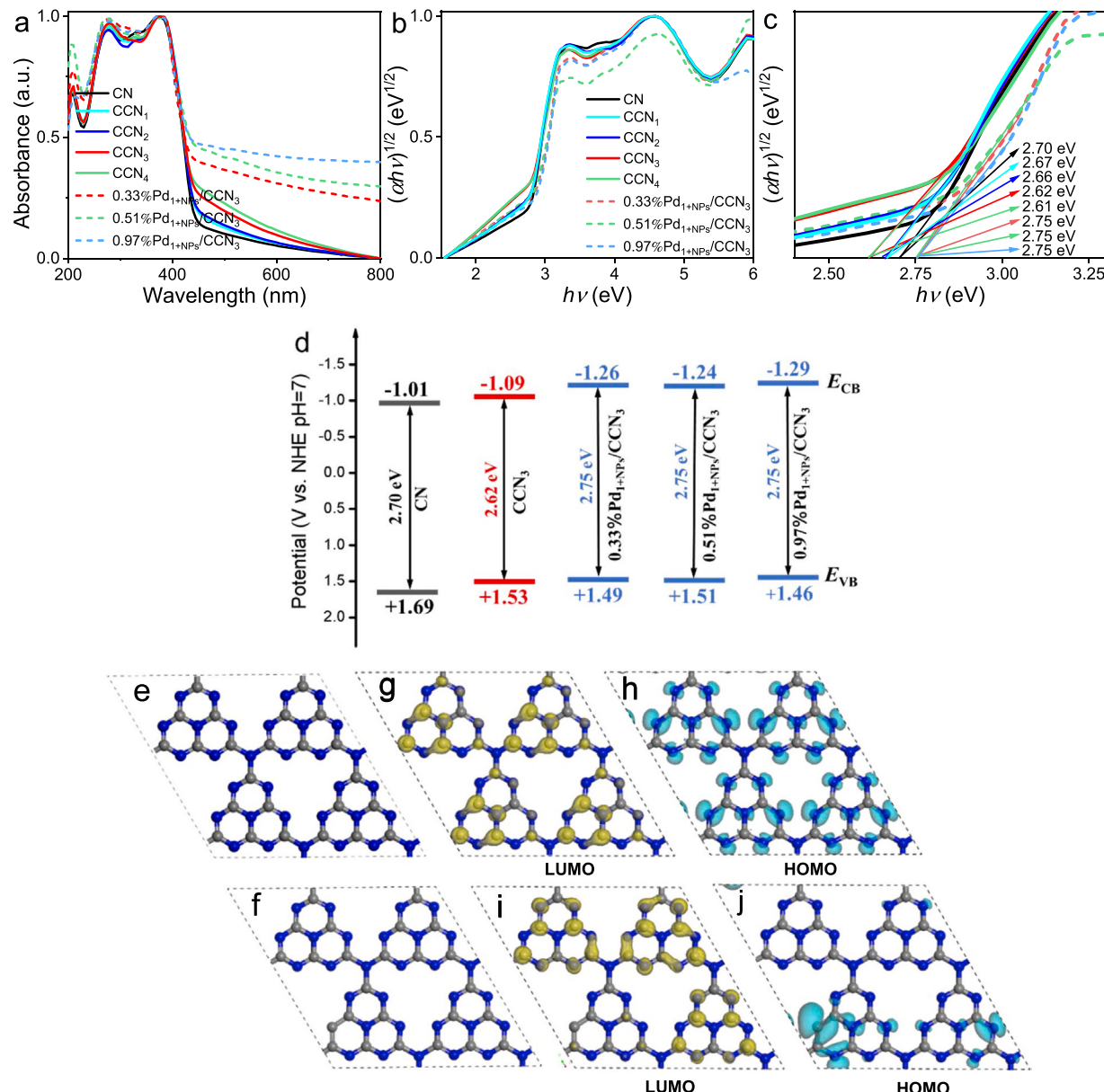


**Fig. 5.** UV-vis/DRS (a), the corresponding transformed Kubelka-Munk function vs. photon energy plots (b, c) and energy band alignments (d) of CN, CCN<sub>3</sub> and Pd<sub>1+NPs</sub>/CCN<sub>3</sub> heterojunctions. The optimized structure models of CN (e) and CCNx (f). The calculated charge density spatial distributions on LUMO and HOMO in (g, h) and CCNx (i, j). Yellow and cyan colors represent the distributions of electrons on LUMO and holes on HOMO.

**Fig. 5a**, CN shows intrinsic optical absorption in region of 200–460 nm, attributing to  $\pi-\pi^*$  electron transition of aromatic C–N heterocycles. After C atom self-doping modification, the absorption edges of four CCNx samples have a slight redshift; additionally, weak absorption in the visible-light region (460–800 nm) emerges, accompanying with the gradually increased visible-light harvesting capacity from CCN<sub>1</sub>, CCN<sub>2</sub>, CCN<sub>3</sub> to CCN<sub>4</sub>. This new light absorption is assigned to the intramolecular charge transfer from electron donor (C<sub>4</sub>N<sub>2</sub> unit) to acceptor (triazine ring). After anchoring Pd species on CCN<sub>3</sub>, the absorption edges of three Pd<sub>1+NPs</sub>/CCN<sub>3</sub> samples show a little blueshift, and the difference of the absorption edge among them is negligible. This absorption edge blueshift thereby is inferred due to the quantum size effect of the introduced single Pd atoms. Additionally, obviously enhanced visible-light harvesting is found in Pd<sub>1+NPs</sub>/CCN<sub>3</sub> samples, and the visible-light harvesting capacity of Pd<sub>1+NPs</sub>/CCN<sub>3</sub> increases gradually with increasing Pd loading level from 0.33, 0.51 to 0.97%. This considerably

strong visible-light absorption is attributed to the surface plasmon resonance effect of Pd nanoparticles [44]. From the plots of the transformed Kubelka–Munk function vs. photon energy (Fig. 5b and c), the bandgap ( $E_g$ ) value of CN (2.70 eV), CCN<sub>1</sub> (2.67 eV), CCN<sub>2</sub> (2.66 eV), CCN<sub>3</sub> (2.62 eV), CCN<sub>4</sub> (2.61 eV), 0.33%Pd<sub>1+NPs</sub>/CCN<sub>3</sub> (2.75 eV), 0.51% Pd<sub>1+NPs</sub>/CCN<sub>3</sub> (2.75 eV) and 0.97%Pd<sub>1+NPs</sub>/CCN<sub>3</sub> (2.75 eV) is estimated, respectively.

To study the changes of conduction band edge potential ( $E_{CB}$ ) and valence band edge potential ( $E_{VB}$ ) of g-C<sub>3</sub>N<sub>4</sub> after C atom self-doping modification and the introduction of Pd species,  $E_{CB}$  values of the above samples are determined by MS method, and the obtained MS plots at different frequencies (1.3, 1.5 and 2.0 kHz) are shown in Fig. S8. The positive tangent slopes of MS plots indicate that the samples are n-type semiconductor, and their  $E_{CB}$  values are equal to the flat band potentials [45,46]. On the basis of  $E_g$  and  $E_{CB}$  values,  $E_{VB}$  values are calculated. Therefore, energy band alignments of various g-C<sub>3</sub>N<sub>4</sub>-based samples are

established (Fig. 5d). It shows that both VB and CB positions of  $\text{CCN}_3$  upshift slightly, in comparison of CN. In the cases of three  $\text{Pd}_{1+\text{NPs}}/\text{CCN}_3$  heterojunctions, their CB position upshifts continuously with respect to  $\text{CCN}_3$  ( $-1.09$  V vs. NHE), namely,  $-1.26$ ,  $-1.24$  and  $-1.29$  V (vs. NHE) for  $0.33\%\text{Pd}_{1+\text{NPs}}/\text{CCN}_3$ ,  $0.51\%\text{Pd}_{1+\text{NPs}}/\text{CCN}_3$  and  $0.97\%\text{Pd}_{1+\text{NPs}}/\text{CCN}_3$ , respectively, while the change of  $E_{\text{VB}}$  value of  $\text{Pd}_{1+\text{NPs}}/\text{CCN}_3$  ( $+1.46$  to  $+1.51$  V vs. NHE) with respect to  $\text{CCN}_3$  ( $+1.53$  V vs. NHE) is ignorable. This more negative CB edge potential of  $\text{Pd}_{1+\text{NPs}}/\text{CCN}_3$  can provide strong driving force for photocatalytic HER.

Based on the optimized structure models of CN (Fig. 5e) and  $\text{CCN}_x$  (Fig. 5f), the charge density spatial distributions on LUMO and HOMO in CN and  $\text{CCN}_x$  structures are calculated. It indicates that after C atom self-doping modifications, the homogeneous distributions of electrons on LUMO and holes on HOMO in CN structure are broken (Fig. 5g and h), and the localized charge density spatial distributions are created (Fig. 5i and j). For  $\text{CCN}_x$ , electrons inhabit on the regions of  $\text{C}_4\text{N}_2$  unit-free heptazine rings in LUMO, while holes mainly localize around  $\text{C}_4\text{N}_2$  unit-contained heptazine rings in HOMO. This localized spatial distribution of holes and electrons in  $\text{CCN}_x$  is anticipated to provide a strong driving force for charge carrier separation.

### 3.2. Photocatalytic $\text{H}_2$ evolution performance of $\text{Pd}_{1+\text{NPs}}/\text{CCN}_x$

The photocatalytic HER performance of  $\text{Pd}_{1+\text{NPs}}/\text{CCN}_x$  is investigated under full solar spectrum and visible-light irradiation, respectively, and  $10\%$  (v/v) TEOA is applied as a hole scavenger. For comparison, the reference catalysts including  $0.26\%\text{Pd}_{\text{NPs}}/\text{CN}$ ,  $0.41\%\text{Pd}_{\text{NPs}}/\text{CCN}_3$  and  $0.34\%\text{Pd}_{\text{NPs}}/\text{CCN}_3$  are also tested under the same conditions. At first, influence of HER temperature on the photocatalytic HER activity is tested by using  $0.33\%\text{Pd}_{1+\text{NPs}}/\text{CCN}_3$  as the representative catalyst. As shown in Fig. 6a, over a period of 240 min full solar spectrum irradiation, the amount of  $\text{H}_2$  produced increases from  $965.4$ ,  $987.2$  to  $1116.8$   $\mu\text{mol}$ , as increasing reaction temperature from  $6$ ,  $10$  to  $15$   $^{\circ}\text{C}$ , originating from the photo-thermal synergistic effect [47]. However, considering the volatilization of TEOA during HER process at higher temperature, current  $\text{H}_2$  evolution reaction is set at  $6$   $^{\circ}\text{C}$ .

Next, HER activity of  $0.26\%\text{Pd}_{\text{NPs}}/\text{CN}$  and four  $\text{Pd}_{1+\text{NPs}}/\text{CCN}_x$  ( $x = 1$ ,  $2$ ,  $3$ , and  $4$ ) heterojunctions obtained at the same theoretical Pd doping level ( $0.5\%$ ) but different C doping levels in  $\text{CCN}_x$  is compared to find out the optimal  $\text{CCN}_x$  support (or C doping level in  $\text{CCN}_x$  support) for the immobilization of single Pd atoms and nanoparticles. As shown in

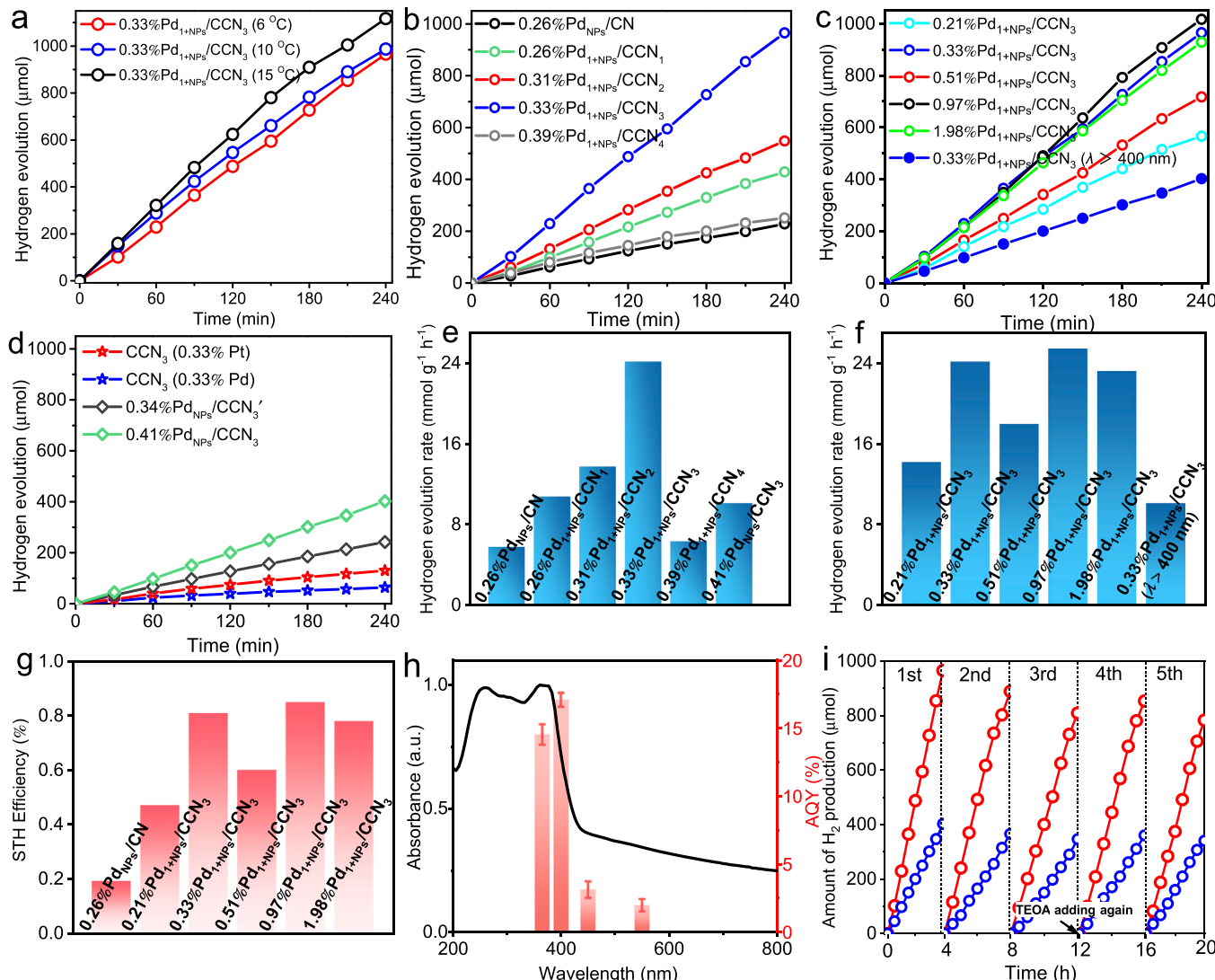


**Fig. 6.** Evaluation of HER performance of  $\text{Pd}_{1+\text{NPs}}/\text{CCN}_x$  heterojunctions. Influence of reaction temperature (a), uracil-to-dicyandiamide molar ratio (b) and Pd doping level (c) on HER activity. Comparison of HER activity of  $\text{CCN}_3$  in homogeneous  $\text{PdCl}_2$  or  $\text{H}_2\text{PtCl}_6$  system as well as reference catalysts (d). The corresponding HER rate of each tested catalyst (e, f). STH efficiency of  $0.33\%\text{Pd}_{1+\text{NPs}}/\text{CCN}_3$  (g). Wavelength-dependent AQY values for HER on  $0.33\%\text{Pd}_{1+\text{NPs}}/\text{CCN}_3$  (h). Photocatalytic stability tests over the  $0.33\%\text{Pd}_{1+\text{NPs}}/\text{CCN}_3$  (i). Red and blue lines represent full solar light spectrum and visible-light irradiation, respectively. Catalyst 10 mg; TEOA 5 mL;  $\text{H}_2\text{O}$  45 mL;  $6$   $^{\circ}\text{C}$ .

**Fig. 6b**, 0.26%Pd<sub>1+NPs</sub>/CCN<sub>1</sub>, 0.31%Pd<sub>1+NPs</sub>/CCN<sub>2</sub>, 0.33%Pd<sub>1+NPs</sub>/CCN<sub>3</sub> and 0.39%Pd<sub>1+NPs</sub>/CCN<sub>4</sub> all exhibit enhanced HER activity than 0.26%Pd<sub>NPs</sub>/CN, and the activity greatly depends on C doping level in CCN<sub>x</sub> support. For example, after full solar spectrum irradiation for 240 min over 0.26%Pd<sub>NPs</sub>/CN, 0.26%Pd<sub>1+NPs</sub>/CCN<sub>1</sub>, 0.31%Pd<sub>1+NPs</sub>/CCN<sub>2</sub>, 0.33%Pd<sub>1+NPs</sub>/CCN<sub>3</sub> and 0.39%Pd<sub>1+NPs</sub>/CCN<sub>4</sub>, the amount of H<sub>2</sub> produced reaches up to 228.1, 428.7, 548.2, 965.4 and 251.3 μmol, respectively. The result reveals the significance of C atom self-doping modification to g-C<sub>3</sub>N<sub>4</sub> for the remarkable improvement of HER activity; more importantly, appropriate C doping level is essential to regulate the optimized electronic structure of g-C<sub>3</sub>N<sub>4</sub> and thus notably enhanced photocatalytic HER activity. According to the above results, by selecting CCN<sub>3</sub> as the most suitable photocatalytically active support, the other four Pd<sub>1+NPs</sub>/CCN<sub>3</sub> heterojunctions are also prepared at theoretical Pd loading level of 0.25, 1.0, 2.0 and 3.0%, and the resulting 0.21%Pd<sub>1+NPs</sub>/CCN<sub>3</sub>, 0.51%Pd<sub>1+NPs</sub>/CCN<sub>3</sub>, 0.97%Pd<sub>1+NPs</sub>/CCN<sub>3</sub> and 1.98%Pd<sub>1+NPs</sub>/CCN<sub>3</sub> together with 0.33%Pd<sub>1+NPs</sub>/CCN<sub>3</sub> are further tested to study the influence of Pd doping level on HER activity of Pd<sub>1+NPs</sub>/CCN<sub>3</sub> catalysts. As displayed in **Fig. 6c**, five Pd<sub>1+NPs</sub>/CCN<sub>3</sub> catalysts all exhibit excellent photocatalytic HER activity, in which 0.33%Pd<sub>1+NPs</sub>/CCN<sub>3</sub> or 0.97%Pd<sub>1+NPs</sub>/CCN<sub>3</sub> performs the best. After 240 min full solar spectrum irradiation, the amount of H<sub>2</sub> produced reaches up to 566.2 (0.21%Pd<sub>1+NPs</sub>/CCN<sub>3</sub>), 965.4 (0.33%Pd<sub>1+NPs</sub>/CCN<sub>3</sub>), 717.9 (0.51%Pd<sub>1+NPs</sub>/CCN<sub>3</sub>), 1017.0 (0.97%Pd<sub>1+NPs</sub>/CCN<sub>3</sub>) and 928.3 μmol (1.98%Pd<sub>1+NPs</sub>/CCN<sub>3</sub>), respectively. The result reflects that both Pd<sub>1</sub> and Pd<sub>NPs</sub> are the reaction active sites that are responsible for excellent photocatalytic HER activity of Pd<sub>1+NPs</sub>/CCN<sub>3</sub>; additionally, Pd<sup>0</sup>-to-Pd<sup>2+</sup> ratio and Pd loading level in the heterojunctions influences the reaction activity in some extent.

The representative 0.33%Pd<sub>1+NPs</sub>/CCN<sub>3</sub> also displays considerably high visible-light ( $\lambda > 400$  nm) photocatalytic HER activity, and the amount of H<sub>2</sub> produced reaches 402.5 μmol after 240 min visible-light irradiation.

For 0.41%Pd<sub>NPs</sub>/CCN<sub>3</sub> and 0.34%Pd<sub>NPs</sub>/CCN<sub>3</sub>', their HER activity is significantly lower than 0.33%Pd<sub>1+NPs</sub>/CCN<sub>3</sub> counterpart, and after full solar spectrum irradiation for 240 min, the amount of H<sub>2</sub> produced reaches 402.5 (0.41%Pd<sub>NPs</sub>/CCN<sub>3</sub>) and 242.2 μmol (0.34%Pd<sub>NPs</sub>/CCN<sub>3</sub>'), respectively (**Fig. 6d**). Therefore, three reference catalysts (0.26%Pd<sub>NPs</sub>/CN, 0.41%Pd<sub>NPs</sub>/CCN<sub>3</sub> and 0.34%Pd<sub>NPs</sub>/CCN<sub>3</sub>') all present notably lower HER activity with respect to 0.33%Pd<sub>1+NPs</sub>/CCN<sub>3</sub>, highlighting the dominated role of as-designed defect engineering strategy to optimize the electronic structure of g-C<sub>3</sub>N<sub>4</sub> by C atom self-doping modification; additionally, although 0.41%Pd<sub>NPs</sub>/CCN<sub>3</sub> has the most suitable CCN<sub>3</sub> support, Pd species are introduced to the support by a conventional NaBH<sub>4</sub> reduction process, and only larger Pd nanoparticles are deposited on the support. The lack of single Pd atoms is the main reason that causes a poor HER activity of 0.41%Pd<sub>NPs</sub>/CCN<sub>3</sub>. The excellent photocatalytic HER activity of 0.33%Pd<sub>1+NPs</sub>/CCN<sub>3</sub> is also indirectly proved by comparison of the activity of CCN<sub>3</sub> in aqueous PdCl<sub>2</sub> or H<sub>2</sub>PtCl<sub>6</sub> solution (the concentration of Pd or Pt element is 0.33%). As displayed in **Fig. 6d**, the amount of H<sub>2</sub> produced is 64.0 (CCN<sub>3</sub> + 0.33% Pd<sup>2+</sup>) and 129.7 μmol (CCN<sub>3</sub> + 0.33% Pt<sup>4+</sup>), respectively, after full solar spectrum irradiation for 240 min, reflecting notably lower HER activity than that of heterogeneous 0.33%Pd<sub>1+NPs</sub>/CCN<sub>3</sub> catalyst. It should be mentioned although Pt shows higher HER activity than Pd, higher price of Pt than Pd makes the former lack of competitiveness from the viewpoint of practical applications.

**Fig. 6e** and **f** present HER rate of each tested catalyst, which demonstrate the same trend with the results shown in **Fig. 6b** and **c**. For two most active catalysts, 0.33%Pd<sub>1+NPs</sub>/CCN<sub>3</sub> and 0.97%Pd<sub>1+NPs</sub>/CCN<sub>3</sub>, under full solar light spectrum irradiation, their HER rate (24.1 and 25.5 mmol g<sup>-1</sup> h<sup>-1</sup>) is 4.2 and 4.5 times higher than that of 0.26%Pd<sub>NPs</sub>/CN (5.70 mmol g<sup>-1</sup> h<sup>-1</sup>); and 2.4 and 2.5 times higher than that of 0.41%Pd<sub>NPs</sub>/CCN<sub>3</sub> (10.06 mmol g<sup>-1</sup> h<sup>-1</sup>). Additionally, under visible-light irradiation, HER rate over the 0.33%Pd<sub>1+NPs</sub>/CCN<sub>3</sub> reaches up to 10.1 mmol g<sup>-1</sup> h<sup>-1</sup>. The determined STH efficiency of the catalysts

is displayed in **Fig. 6g**, indicating higher STH efficiency of five Pd<sub>1+NPs</sub>/CCN<sub>3</sub> heterojunctions (0.47, 0.81, 0.60, 0.85 and 0.71% for 0.21%Pd<sub>1+NPs</sub>/CCN<sub>3</sub>, 0.33%Pd<sub>1+NPs</sub>/CCN<sub>3</sub>, 0.51%Pd<sub>1+NPs</sub>/CCN<sub>3</sub>, 0.97%Pd<sub>1+NPs</sub>/CCN<sub>3</sub> and 1.98%Pd<sub>1+NPs</sub>/CCN<sub>3</sub>, respectively) in comparison of 0.26%Pd<sub>NPs</sub>/CN (0.19%).

Taking 0.33%Pd<sub>1+NPs</sub>/CCN<sub>3</sub> as the representative catalyst, the photoelectric efficiency of Pd<sub>1+NPs</sub>/CCN<sub>x</sub> is evaluated by the determination of AQY values under different monochromatic light irradiation supplied by a Xe lamp equipped with different band-pass filters. Considering the influence of the concentration of 0.33%Pd<sub>1+NPs</sub>/CCN<sub>3</sub> on the amount of H<sub>2</sub> produced and the incident irradiation [**19**], the catalyst concentration-dependent AQY values are determined under 365, 400, 450 and 550 nm monochromatic light irradiation, respectively. As can be seen in **Fig. S9**, the amount of H<sub>2</sub> produced reaches up to a plateau at 0.33%Pd<sub>1+NPs</sub>/CCN<sub>3</sub> concentration of 0.4 (365 nm), 0.5 (400 nm), 0.5 (450 nm) and 0.7 g L<sup>-1</sup> (550 nm), respectively, which is caused by the saturation of light absorption. At the above each stationary point, the actual photoelectric efficiency of 0.33%Pd<sub>1+NPs</sub>/CCN<sub>3</sub> that represented by AQY is 14.6 (365 nm), 17.1 (400 nm), 3.16 (450 nm) and 1.98% (550 nm), respectively (**Fig. 6h**). This AQY value change trend implies a good correlation with the light absorption properties of 0.33%Pd<sub>1+NPs</sub>/CCN<sub>3</sub>, suggesting the intrinsic transition-governed H<sub>2</sub> production behavior; moreover, considerably high AQY values at 450 and 550 nm are of great significance for 0.33%Pd<sub>1+NPs</sub>/CCN<sub>3</sub> to maximize the utilization of photons in visible-light region. Additionally, in comparison of AQY values reported recently in typical photocatalytic HER systems, the AQY value of 0.33%Pd<sub>1+NPs</sub>/CCN<sub>3</sub> is comparable to or surpasses that of these photocatalytic systems (**Table S3**).

In addition to its exceptional HER activity, the photocatalytic stability is also a crucial factor to evaluate the HER performance of Pd<sub>1+NPs</sub>/CCN<sub>x</sub> heterojunctions. The long-term stability is therefore tested on the representative 0.33%Pd<sub>1+NPs</sub>/CCN<sub>3</sub> catalyst under both full solar light spectrum and visible-light irradiation. As shown in **Fig. 6i**, 0.33%Pd<sub>1+NPs</sub>/CCN<sub>3</sub> demonstrates a stable HER activity under visible-light irradiation during five catalytic cycles, and the amount of H<sub>2</sub> produced is 402.5 (1st), 365.7 (2nd), 346.5 (3rd), 360.6 (4th) and 340.5 μmol (5th), respectively; under full solar light spectrum irradiation, the amount of H<sub>2</sub> produced is 965.4 (1st), 898.8 (2nd), 809.2 (3rd), 853.5 (4th) and 782.8 μmol (5th), respectively. Somewhat decrease of HER activity is found in the third run, caused by the used up of TEOA because of more plentiful holes are generated under full solar light spectrum irradiation. After supplying 5 mL of TEOA in the reaction system, the HER activity restores almost. Therefore, Pd<sub>1+NPs</sub>/CCN<sub>x</sub> heterojunctions show satisfactory photocatalytic HER stability.

Ultimately, isotope-labeled experiment is carried out to find out the origin of the generated H<sub>2</sub> in a 0.33%Pd<sub>1+NPs</sub>/CCN<sub>3</sub>/TEOA photocatalytic system. As displayed in **Fig. S11a** and **b**, only one peak emerges in GC effluent curves of the HER product in H<sub>2</sub>O and D<sub>2</sub>O systems, respectively. Therefore, it is confirmed that H<sub>2</sub> (D<sub>2</sub>) is produced solely from the photocatalytic H<sub>2</sub>O (D<sub>2</sub>O) splitting rather than other effects. Further HER activity test indicates that photocatalytic reduction of H<sub>2</sub>O (D<sub>2</sub>O) over the 0.33%Pd<sub>1+NPs</sub>/CCN<sub>3</sub> can produce the same amount of H<sub>2</sub> or D<sub>2</sub> almost (**Fig. S11c**).

### 3.3. Photocatalytic HER mechanism over the Pd<sub>1+NPs</sub>/CCN<sub>x</sub>

To reveal the correlation between Pd<sub>1+NPs</sub>/CCN<sub>x</sub> structure and photocatalytic HER performance and to gain a deep and comprehensive insight into the Pd<sub>1+NPs</sub>/CCN<sub>x</sub>-assisted photocatalytic HER mechanism, both important factors, namely, thermodynamic requirement and dynamic efficiency, are considered. Thermodynamically, both C atom-self doping modification and Pd<sub>1</sub> and Pd<sub>NPs</sub> co-anchoring have a little influence on the E<sub>g</sub> value of g-C<sub>3</sub>N<sub>4</sub> (2.75 eV vs. 2.70 eV, **Fig. 5c**), suggesting that Pd<sub>1+NPs</sub>/CCN<sub>x</sub> and CN can be activated by the same photon energy; moreover, Pd<sub>1+NPs</sub>/CCN<sub>x</sub> also show moderate absorption in visible-light region, which can photoexcite more electrons and holes

under full solar spectrum or visible-light irradiation. On the other hand,  $\text{Pd}_{1+\text{NPs}}/\text{CCN}_x$  heterojunctions possess more negative  $E_{\text{CB}}$  value than CN or  $\text{CCN}_x$  (Fig. 5c), reflecting more strong HER driving force. Therefore,  $\text{Pd}_{1+\text{NPs}}/\text{CCN}_x$  heterojunctions are thermodynamically more favorable for photocatalytic HER process.

Apart from sufficient light absorption and suitable CB edge potential, efficient photon utilization efficiency is more important for photocatalytic HER process, which depends on charge carrier separation and transport dynamics. To investigate charge carrier separation and transport dynamics of  $\text{Pd}_{1+\text{NPs}}/\text{CCN}_x$  heterojunctions, following experiments combined with DFT calculations are conducted. First, steady-state PL spectra are recorded to unveil the radiative recombination of charge carriers in CN,  $\text{CCN}_3$  and three  $\text{Pd}_{1+\text{NPs}}/\text{CCN}_3$  heterojunctions. From the steady-state PL emission spectra displayed in Fig. 7a it is found that CN exhibits a strong band edge PL emission peak at 444 nm, suggesting its considerably high radiative recombination probability. For  $\text{CCN}_3$ , the emission peak redshifts to 456 nm, originating from the extended  $\pi$ -electron delocalization; additionally, the emission peak intensity decreases dramatically, indicating that C atom self-doping modification can effectively prevent the radiative recombination of charge carriers. Continuously decreased emission peak intensity is found in  $\text{Pd}_{1+\text{NPs}}/\text{CCN}_3$ , and PL quenching enhances gradually with the increment of Pd loading level from 0.33, 0.51 to 0.97%; however, the position of emission peak of  $\text{Pd}_{1+\text{NPs}}/\text{CCN}_3$  is the same as that of  $\text{CCN}_3$ . Therefore, charge carrier recombination in  $\text{g-C}_3\text{N}_4$  is inhibited significantly after C atom-self doping modification and  $\text{Pd}_1$  and  $\text{Pd}_{\text{NPs}}$  co-anchoring, which renders to effective survival of the excited states and thus a high population of photoexcited electrons and holes. TRPD spectra shown in Fig. 7b demonstrate the consistent PL decay trend with that of steady-state PL spectra, and the calculated average PL lifetime decay ( $\tau_{\text{av}}$ ) value of CN,  $\text{CCN}_3$ , 0.33% $\text{Pd}_{1+\text{NPs}}/\text{CCN}_3$ , 0.51% $\text{Pd}_{1+\text{NPs}}/\text{CCN}_3$  and 0.97% $\text{Pd}_{1+\text{NPs}}/\text{CCN}_3$  is 7.23, 7.11, 6.97, 6.77 and 6.38 ns, respectively, on the basis of biexponential decay function. The steadily declined PL lifetime decay of  $\text{Pd}_{1+\text{NPs}}/\text{CCN}_3$  with respect to  $\text{CCN}_3$  implies further boosted charge carrier separation and transport dynamics after co-anchoring  $\text{Pd}_1$  and  $\text{Pd}_{\text{NPs}}$  on  $\text{CCN}_3$ .

The charge carrier separation and transport dynamics of  $\text{Pd}_{1+\text{NPs}}/\text{CCN}_3$

are further evaluated by the photoelectrochemical measurements. As shown in Fig. 7c, in a dilute  $\text{Na}_2\text{SO}_4$  aqueous solution, each working electrode can generate a TP response rapidly under Xe lamp irradiation, and the generated TP response is stable enough during five on-off intermittent irradiation cycles. Compared with CN,  $\text{CCN}_3$  can produce obviously stronger TP response. Further dramatically increased TP response is obtained on three  $\text{Pd}_{1+\text{NPs}}/\text{CCN}_3$  heterojunctions, and they follow TP response trend of  $0.51\%\text{Pd}_{1+\text{NPs}}/\text{CCN}_3 \approx 0.33\%\text{Pd}_{1+\text{NPs}}/\text{CCN}_3 < 0.97\%\text{Pd}_{1+\text{NPs}}/\text{CCN}_3$ . For the 0.97% $\text{Pd}_{1+\text{NPs}}/\text{CCN}_3$ , its TP density is nearly 7 times higher than that of CN. The measured EIS Nyquist plots coincide with the above TP response result. As depicted in Fig. 7d, five working electrodes exhibit continuously reduced curvature diameter of Nyquist cycles from CN,  $\text{CCN}_3$ , 0.51% $\text{Pd}_{1+\text{NPs}}/\text{CCN}_3$ , 0.33% $\text{Pd}_{1+\text{NPs}}/\text{CCN}_3$  to 0.97% $\text{Pd}_{1+\text{NPs}}/\text{CCN}_3$ . Since a smaller curvature diameter of Nyquist cycle corresponds to smaller charge carrier transfer resistance, 0.97% $\text{Pd}_{1+\text{NPs}}/\text{CCN}_3$  exhibits the smallest charge transfer resistance among the tested samples.

Both the above PL and photoelectrochemical tests evidence that suitable C atom self-doping modification can effectively facilitate the separation and transport of the photogenerated charge carriers in  $\text{Pd}_{1+\text{NPs}}/\text{CCN}_3$ ; more importantly, the charge carrier separation and transport dynamics is further notably boosted after co-anchoring of  $\text{Pd}_1$  and  $\text{Pd}_{\text{NPs}}$  on  $\text{CCN}_x$ . To explain the effect of C atom self-doping modification on the electronic structure of  $\text{CCN}_x$ , ESP surface distributions of CN (Fig. 7e) and  $\text{CCN}_x$  (Fig. 7f) are calculated based on the optimized structure models of CN (Fig. 5d) and  $\text{CCN}_x$  (Fig. 5e). In comparison of CN with evenly distributed electrons around triangular edges neighboring to N atoms (red color regions) and holes on the other regions (blue color regions), the localized charge accumulation happens in  $\text{CCN}_x$ . Namely, electrons prefer to accumulate around the edges neighboring to N atoms in two triazine rings, while holes aggregate around  $\text{C}_4\text{N}_2$  unit neighboring to C atoms. This localized charge carrier distribution induces a molecular dipole in  $\text{CCN}_x$  ( $\mu = 1.3$  D). Combination of ESP analysis with the charge density spatial distributions on LUMO and HOMO in CN and  $\text{CCN}_x$  structures (Fig. 5f–i) it is concluded that the localized charge density spatial distribution in  $\text{CCN}_x$  leads to the directional migration of electrons and holes in heptazine rings driven by the local electric field,

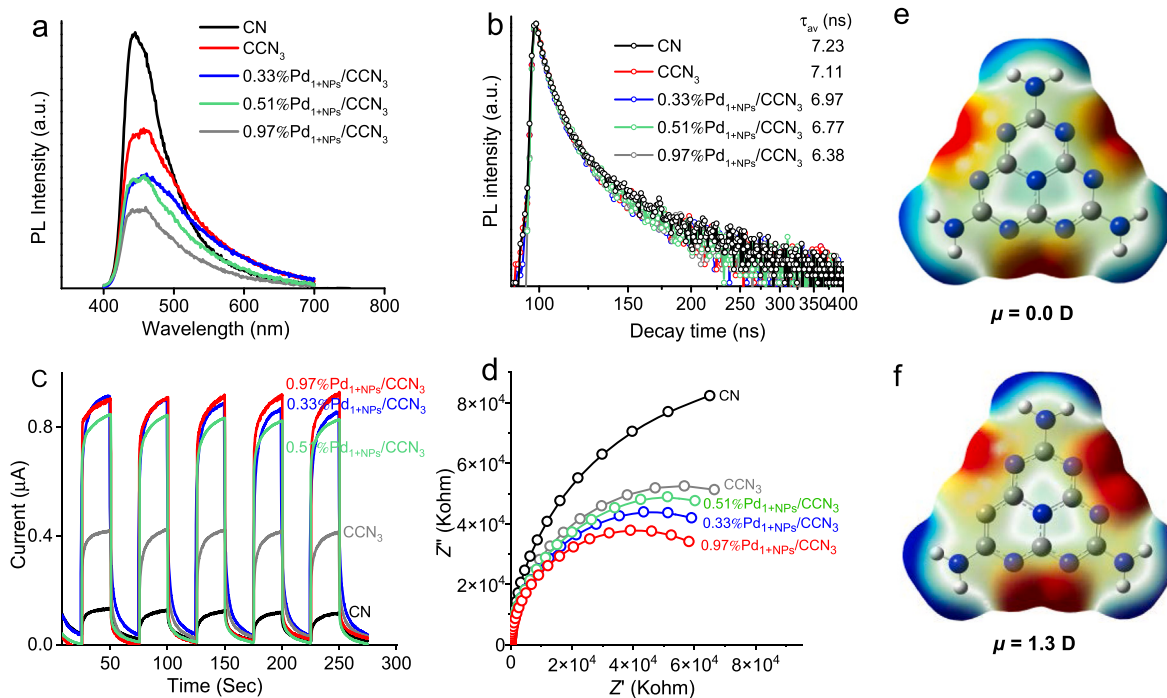


**Fig. 7.** Steady-state PL emission (a) and TRPD spectra (b). TP responses (c) and EIS Nyquist plots (d) of CN, CCN and  $\text{Pd}_{1+\text{NPs}}/\text{CCN}_3$  heterojunctions. ESP distribution of CN (e) and  $\text{CCN}_x$  (f).

accordingly, charge carrier separation and transport dynamics is facilitated. It should be noted that much higher C doping level may produce new electron-hole recombination centers via deep trapping, which in turn leads to the loss of some free electrons. Therefore, among 0.26% Pd<sub>1+NPs</sub>/CCN<sub>1</sub>, 0.31%Pd<sub>1+NPs</sub>/CCN<sub>2</sub>, 0.33%Pd<sub>1+NPs</sub>/CCN<sub>3</sub> and 0.39% Pd<sub>1+NPs</sub>/CCN<sub>4</sub> heterojunctions, 0.39%Pd<sub>1+NPs</sub>/CCN<sub>4</sub> shows the lowest photocatalytic HER activity.

The role of co-anchored Pd<sub>1</sub> and Pd<sub>NPs</sub> on the charge carrier separation and transport dynamics of Pd<sub>1+NPs</sub>/CCN<sub>x</sub> is further clarified forcefully by comparison of in-situ fs-TA spectroscopy analysis results of CCN<sub>3</sub> and 0.33%Pd<sub>1+NPs</sub>/CCN<sub>3</sub>. From time-dependent 3D contour plots of fs-TA spectra shown in Fig. 8a and b it is found that both CCN<sub>3</sub> and 0.33%Pd<sub>1+NPs</sub>/CCN<sub>3</sub> exhibit a small part of negative signal below 480 nm and predominant positive signal over 480 nm; moreover, the 0.33%Pd<sub>1+NPs</sub>/CCN<sub>3</sub> possesses stronger signals than CCN<sub>3</sub>. This negative signal corresponds to the stimulated emission (SE) [48,49]. SE mainly facilitates the recombination of electrons and holes, which negatively affects HER activity. The positive signal is associated with the excited-state absorption (ESA) process of electrons, holes or electron-hole pairs, and strong ESA signal signifies fast separation and transport dynamics of charge carriers and thus the positive contribution to improving HER activity [50]. To study the spectral evolution kinetics, the absorption decay of CCN<sub>3</sub> and 0.33%Pd<sub>1+NPs</sub>/CCN<sub>3</sub> from fs-TA spectra at different probe delays (from 1.4 ps to 1 ns) is provided (Fig. 8c and d), which shows continuous absorption decay from 1.4 ps to 1 ns on both samples; moreover, in comparison of CCN<sub>3</sub>, 0.33%Pd<sub>1+NPs</sub>/CCN<sub>3</sub> exhibits broader and notably enhanced ESA signal intensities, highlighting the obviously improved charge carrier separation and transport dynamics induced by co-anchoring of Pd<sub>1</sub> and Pd<sub>NPs</sub> on CCN<sub>3</sub>. To monitor the kinetics decay process of ESA, fs-TA kinetic decay traces of CCN<sub>3</sub> and 0.33%Pd<sub>1+NPs</sub>/CCN<sub>3</sub> are fitted at the representative wavelengths, 603 and 653 nm, based on tri-exponential decay function

(Fig. 8e and f), and the fitting time parameters ( $\tau_1$ ,  $\tau_2$  and  $\tau_3$ ) of fs-TA decay are summarized in Table S4. The parameters of  $\tau_1$ ,  $\tau_2$  and  $\tau_3$  are related to charge carrier recombination, shallow charge carrier trapping and deep charge carrier trapping process, respectively. Deep charge carrier trapping is generally a long process with large  $\tau_3$  value, and thereby charge carrier recombination and shallow charge carrier trapping are the main concerned parameters to clarify the kinetics decay process of SEA. At 603 nm, three fitted time parameters are 0.19 ( $\tau_1$ , 48%), 3.33 ( $\tau_2$ , 27%) and 69.2 ps ( $\tau_3$ , 25%) for CCN<sub>3</sub>; and 0.68 ( $\tau_1$ , 44%), 7.82 ( $\tau_2$ , 32%) and 150.9 ps ( $\tau_3$ , 2%) for 0.33%Pd<sub>1+NPs</sub>/CCN<sub>3</sub>. At 653 nm, the parameters are 0.06 ( $\tau_1$ , 30%), 0.69 ( $\tau_2$ , 42%) and 81.7 ps ( $\tau_3$ , 28%) for CCN<sub>3</sub>; and 0.28 ( $\tau_1$ , 32%), 4.91 ( $\tau_2$ , 49%) and 153.78 ps ( $\tau_3$ , 19%) for 0.33%Pd<sub>1+NPs</sub>/CCN<sub>3</sub>. The long-lived charge carrier recombination and shallow charge trapping as well as enlarged proportion of  $\tau_1$  or  $\tau_2$  on total time decay are both indicate effective SEA survival, which finally provides more abundant free electrons for HER process. Accordingly, 0.33%Pd<sub>1+NPs</sub>/CCN<sub>3</sub> with much larger  $\tau_1$  and  $\tau_2$  values as well as higher  $\tau_1$  and  $\tau_2$  proportion than CCN<sub>3</sub> clearly shows a slower charge carrier recombination dynamics and longer-lived shallow charge carrier trapping processes. The results finally lead to long lifetime of charge carriers, in which the long-lived photogenerated electrons play the dominated role to significantly enhance HER activity. The results coincide with those of the above photoluminescence and photoelectrochemical measurements.

The calculated charge density difference (CDD) distributions of CCN<sub>x</sub>-immobilized Pd<sub>1</sub> (Pd<sub>1</sub>/CCN<sub>x</sub>) and CCN<sub>x</sub>-immobilized Pd<sub>1</sub> and Pd<sub>NPs</sub> (Pd<sub>1+NPs</sub>/CCN<sub>x</sub>) based on structural models illustrated in Fig. 4d and g can strongly support the above experimental results. CDD provides charge carrier density redistributions on the catalysts after being photoexcited from ground state (S<sub>0</sub>) to the first excited state (S<sub>1</sub>). The CDD of Pd<sub>1</sub>/CCN<sub>x</sub> indicates that most of the photoexcited electrons distribute around single Pd atoms (yellow regions in Fig. 9a);

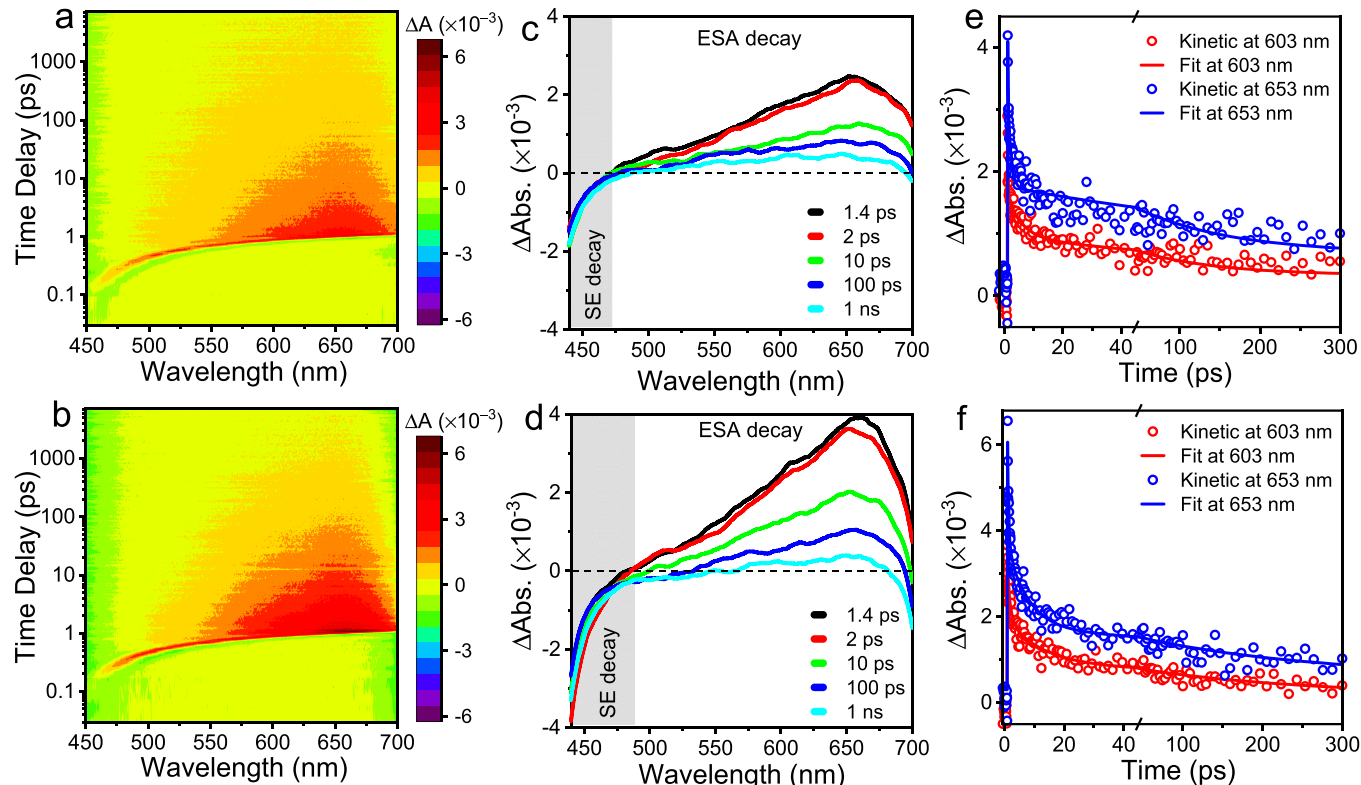


**Fig. 8.** Photogenerated charge carrier dynamics analysis by fs-TA spectroscopy (pump laser 370 nm). Time-dependent 3D contour plots of fs-TA spectra for CCN<sub>3</sub> (a) and 0.33%Pd<sub>1+NPs</sub>/CCN<sub>3</sub> (b) in the initial time window of 8 ns. The representative absorption decay (Abs.) from fs-TA spectra at different probe delays for CCN<sub>3</sub> (c) and 0.33%Pd<sub>1+NPs</sub>/CCN<sub>3</sub> (d). Kinetics decay process from fs-TA spectra observed at 603 and 653 nm for CCN<sub>3</sub> (e) and 0.33%Pd<sub>1+NPs</sub>/CCN<sub>3</sub> (f) and their corresponding tri-exponential decay curves.

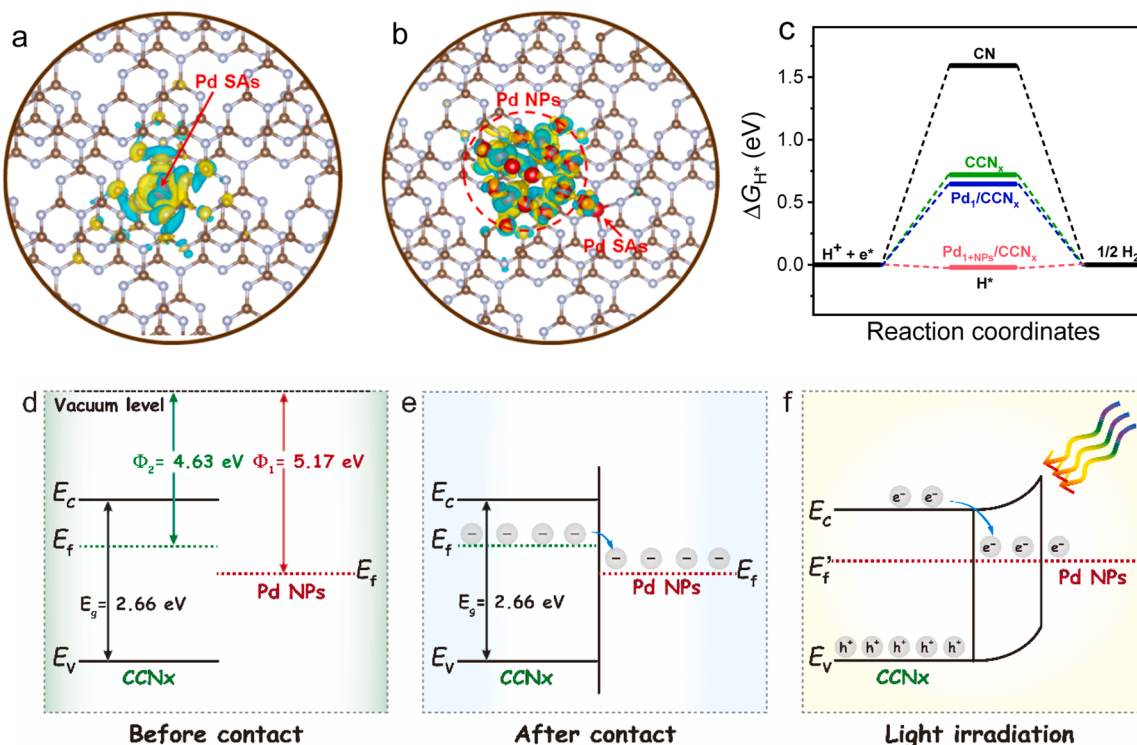


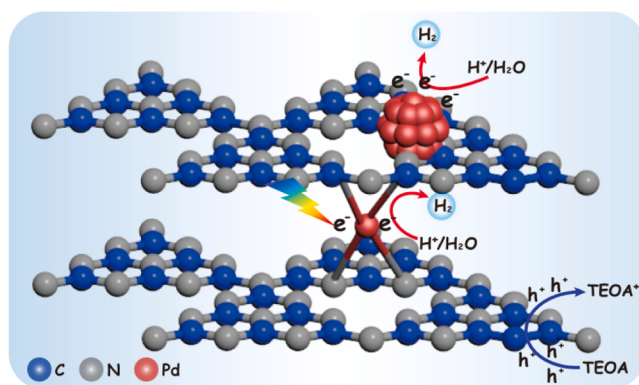
**Fig. 9.** Charge density difference analysis. Yellow and cyan regions refer to the accumulation and depletion of electrons during S<sub>0</sub>-S<sub>1</sub> transition of Pd<sub>1</sub>/CCN<sub>x</sub> (a) and Pd<sub>1+NPs</sub>/CCN<sub>x</sub> (b). The calculated Gibbs free energy diagrams for HER on CN, CCN<sub>x</sub>, Pd<sub>1</sub>/CCN<sub>x</sub> and Pd<sub>1+NPs</sub>/CCN<sub>x</sub> (c). Band structure before (d) and after (e) contact between metallic Pd<sup>0</sup> nanoparticles and CCN<sub>x</sub>. (f) Electron transfer mechanism between CCN<sub>x</sub> and the anchored Pd<sup>0</sup> nanoparticles in Pd<sub>1+NPs</sub>/CCN<sub>x</sub> heterojunctions.

additionally, other small part of electrons situate at the heptazine rings adjacent to Pd<sub>1</sub>. The CDD of Pd<sub>1+NPs</sub>/CCN<sub>x</sub> displays an interesting and optimized distribution of the photoexcited electrons, and all of the photoexcited electrons are totally captured by both single Pd atoms and Pd nanoparticles sites (yellow regions in Fig. 9b). Therefore, extremely higher population of free photoexcited electrons are generated in Pd<sub>1+NPs</sub>/CCN<sub>x</sub> system with respect to Pd<sub>1</sub>/CCN<sub>x</sub> for HER process.

Ultimately, Gibbs free energy ( $\Delta G_{H^*}$ ) of CN, CCN<sub>x</sub>, Pd<sub>1</sub>/CCN<sub>x</sub> and Pd<sub>1+NPs</sub>/CCN<sub>x</sub> is respectively calculated to further unveil the prominent synergistic effect of Pd<sub>1</sub> and small Pd<sub>NPs</sub> for the notably enhanced HER activity. As shown in Fig. 9c, the energy barrier of activation of the intermediate species (H<sup>\*</sup>) to produce H<sub>2</sub> notably decreases from CN, CCN<sub>x</sub>, Pd<sub>1</sub>/CCN<sub>x</sub> to Pd<sub>1+NPs</sub>/CCN<sub>x</sub> catalyst. For CN, a largely positive  $\Delta G_{H^*}$  value (1.59 eV) indicates extremely weak chemical adsorption to H<sup>\*</sup> and low desorption to H<sub>2</sub>, highlighting the high energy barrier for HER process. In the case of CCN<sub>x</sub>, the  $\Delta G_{H^*}$  value decreases to 0.72 eV, suggesting the significance of C atom self-doping modification for adjusting the electronic structure of g-C<sub>3</sub>N<sub>4</sub> and thus the ameliorated H<sup>\*</sup> chemical adsorption and H<sub>2</sub> desorption process. After the introduction of Pd species, the  $\Delta G_{H^*}$  value reduces continuously, namely, 0.64 (Pd<sub>1</sub>/CCN<sub>x</sub>) and -0.02 eV (Pd<sub>1+NPs</sub>/CCN<sub>x</sub>), respectively. The result is caused by the migration of electrons from sp<sup>2</sup>-hybridized N atoms in CCN<sub>x</sub> to d orbitals of Pd atoms, which remarkably reduces the energy barrier of H<sup>\*</sup> activation by strengthening H<sup>\*</sup> chemical adsorption. Particularly, the lowest energy barrier on Pd<sub>1+NPs</sub>/CCN<sub>x</sub> (close to zero) strongly suggests that both Pd<sub>1</sub> and small Pd<sub>NPs</sub> act as the electron-trapping sites or HER centers to remarkably promote the spontaneous H<sup>\*</sup> chemical adsorption and H<sub>2</sub> desorption, corresponding to significantly decreased H<sup>\*</sup> activation energy barrier and thereby higher HER activity in comparison of the Pd<sub>1</sub>/CCN<sub>x</sub> counterpart.

The above theoretical simulation powerfully confirms that Pd<sub>1</sub> and Pd<sub>NPs</sub> co-anchored on CCN<sub>x</sub> can effectively capture more abundant photoexcited electrons to join in HER process, giving rise to significantly enhanced HER activity. Combination of extensive characterizations with

theoretical simulation, photocatalytic HER mechanism over the Pd<sub>1+NPs</sub>/CCN<sub>x</sub> is proposed. As illustrated in Scheme 1, under full solar light spectrum or visible-light irradiation on Pd<sub>1+NPs</sub>/CCN<sub>x</sub>, a mass of photoexcited electron-hole pairs are generated. Driven by following factors, sluggish charge carrier separation and transport dynamics on CN is remarkably boosted, which ultimately creates long-lived free photo-generated electrons for notably enhanced HER activity (holes are quenched by TEOA). On the one hand, C atom self-doped modification-induced local electric field can effectively promote the separation and transport of electron-hole pairs. On the other, as-formed interlayer N-Pd-N bridge coordination bonds build an atomic-scale electron transfer channel in Pd<sub>1+NPs</sub>/CCN<sub>x</sub> to guide electron migration between the adjacent heptazine rings, leading to lots of electrons are captured by single Pd atoms. This is the main contribution of single Pd atoms to the notably boosted charge carrier separation and transport dynamics on CCN<sub>x</sub> and thus the improved photocatalytic HER activity.



**Scheme 1.** The proposed photocatalytic HER mechanism over the Pd<sub>1+NPs</sub>/CCN<sub>x</sub> heterojunctions.

Simultaneously, for the co-anchored in-plane small metallic Pd<sup>0</sup> nanoparticles, they show unique Mott–Schottky effect, which can increase the number of electrons around them [51,52]. To confirm the Mott–Schottky interactions between metallic Pd<sup>0</sup> nanoparticles and CCN<sub>x</sub> support, DFT calculations are applied to obtain work function ( $\phi$ ) values of CCN<sub>x</sub> and Pd nanoparticles (Fig. S10). As shown in Fig. 9d, Pd nanoparticles has a higher work function ( $\phi_1 = 5.17$  eV) and lower Fermi level values, whereas CCN<sub>x</sub> shows a lower work function ( $\phi_2 = 4.63$  eV) and higher Fermi level values. Since the presence of difference in work function or Fermi level value between Pd nanoparticles and CCN<sub>x</sub>, electrons on Fermi level of CCN<sub>x</sub> spontaneously flow to Fermi level of Pd nanoparticles once two components contact each other (Fig. 9e). Under full solar spectrum or visible-light irradiation, the photoexcited electrons continuously transfer to Fermi level of Pd nanoparticles until the Fermi level of CCN<sub>x</sub> and Pd nanoparticles coincide and form Schottky barrier (Fig. 9f); meanwhile, band edges of CCN<sub>x</sub> bend upward due to the electron depletion. As-formed Schottky barrier notably inhibits the recombination of photogenerated charges and facilitates the transportation of electrons to Pd nanoparticles effectively.

According to the above discussion, the synergy of as-built interlayer N–Pd–N electron transfer channels at the atomic-scale and surface Mott–Schottky effect of metallic Pd nanoparticles significantly accelerates migration of photogenerated electrons not only in interlayer of CCN<sub>x</sub> but also at the interface between Pd nanoparticles and CCN<sub>x</sub>, which leads to plentiful electrons accumulating around single Pd atoms and Pd nanoparticles active sites to significantly decrease the energy barrier of H<sup>\*</sup> activation and boost HER photodynamics greatly. This is the most important factor to the surface photocatalytic HER process. Among five Pd<sub>1+NPs</sub>/CCN<sub>3</sub> heterojunctions, 0.97%Pd<sub>1+NPs</sub>/CCN<sub>3</sub> or 0.33%Pd<sub>1+NPs</sub>/CCN<sub>3</sub> with the most suitable Pd<sup>0</sup>-to-Pd<sup>2+</sup> ratio and Pd loading level shows the most effective synergy and thus the most abundant photogenerated electrons for the surface photocatalytic HER process. The lowest HER activity of 0.21%Pd<sub>1+NPs</sub>/CCN<sub>3</sub> is attributed to too low Pd loading level (and thus limited active sites) and the lack of small Pd nanoparticles. Although 1.98%Pd<sub>1+NPs</sub>/CCN<sub>3</sub> has the highest Pd loading level, its HER activity is not elevated further in comparison of 0.97%Pd<sub>1+NPs</sub>/CCN<sub>3</sub>, which is attributed to unsuitable Pd<sup>0</sup>-to-Pd<sup>2+</sup> ratio (i.e., 3.29, estimated by Pd XPS shown in Fig. S12) and enlarged size of Pd nanoparticles (Fig. S2b). Much higher proportion of Pd nanoparticles together with the enlarged size in 1.98%Pd<sub>1+NPs</sub>/CCN<sub>3</sub> heterojunction inevitably increase the recombination probability of the photoexcited charge carriers and thus the limited photocatalytic HER activity [53]. As for 0.51%Pd<sub>1+NPs</sub>/CCN<sub>3</sub>, its somewhat lower HER activity than 0.33%Pd<sub>1+NPs</sub>/CCN<sub>3</sub> or 0.97%Pd<sub>1+NPs</sub>/CCN<sub>3</sub> is possibly also caused by unsuitable Pd<sup>0</sup>-to-Pd<sup>2+</sup> ratio.

At last, single Pd atoms with specific coordinatively unsaturated sites and unique electronic structures can provide enormous surface active sites and thus the maximum Pd atoms utilization efficiency for HER.

Since co-anchoring Pd single atoms and small nanoparticles on CCN<sub>x</sub> also increase the reduction driven force by increasing CB edge potential, both photodynamics and thermodynamic driving forces are improved in Pd<sub>1+NPs</sub>/CCN<sub>x</sub> heterojunctions, which finally results in their superior HER activity than Pd<sub>NPs</sub>/CN, Pd<sub>NPs</sub>/CCN<sub>x</sub> and Pd<sub>NPs</sub>/CCN<sub>x</sub>, respectively.

#### 4. Conclusions

Supramolecule self-assembly of dicyandiamide with  $\pi$ -electron-rich uracil followed by thermal polymerization route is developed to prepare C atom self-doped g-C<sub>3</sub>N<sub>4</sub> (CCN<sub>x</sub>), in which supramolecule self-assembly is a essential preorganization step to optimize the molecular structure of CCN<sub>x</sub>; meanwhile, C doping level is controllable precisely by adjusting uracil-to-dicyandiamide molar ratio. CCN<sub>x</sub> is an ideal photocatalytically active support for co-anchoring of single Pd atoms by the interlayer Pd–N coordination bonding and small Pd nanoparticles on the in-plane of CCN<sub>x</sub> by interfacial Pd–N/C interaction. After optimizing C doping

level, the prepared Pd<sub>1+NPs</sub>/CCN<sub>3</sub> heterojunctions all exhibit significantly enhanced photocatalytic HER activity. Thermodynamically, the reduction driven force is increased after C atom self-doping modification by lifting CB position. More importantly, photon utilization efficiency is improved by dramatically boosted charge carrier separation and transport dynamics, originating from the synergy of as-built interlayer N–Pd–N electron transfer channels at the atomic-scale and unique Mott–Schottky effect of small Pd nanoparticles. The facilitated thermodynamics and photodynamics together with the maximum Pd atoms utilization efficiency ultimately create long-lived free photogenerated electrons for notably enhanced HER activity. This work demonstrates new insights into the construction and mechanism understanding of defect-modified g-C<sub>3</sub>N<sub>4</sub>-co-anchored single Pd atoms and small Pd nanoparticles for notably enhanced HER activity.

#### CRediT authorship contribution statement

**Ren Miao:** Data curation, Formal analysis, Investigation, Writing – original draft. **Meng Jiaqi:** Data curation, Funding acquisition. **Yang Yuxin:** Conceptualization, Methodology. **Zhang Xueyan:** Formal analysis. **Yang Guang:** Visualization. **Qin Lang:** Validation. **Guo Yihang:** Funding acquisition, Resources, Writing – review & editing.

#### Declaration of Competing Interest

The authors declare that they have no known competing financial interests or personal relationships that could have appeared to influence the work reported in this paper.

#### Data availability

Data will be made available on request.

#### Acknowledgements

This work is financially supported by the National Natural Science Foundation of China (22072016, 52270061 and 52300078).

#### Appendix A. Supporting information

Supplementary data associated with this article can be found in the online version at doi:10.1016/j.apcatb.2023.123680.

#### References

- [1] R. Chen, Z. Ren, Y. Liang, G. Zhang, T. Dittrich, R. Liu, Y. Liu, Y. Zhao, S. Pang, H. An, C. Ni, P. Zhou, K. Han, F. Fan, C. Li, Spatiotemporal imaging of charge transfer in photocatalyst particles, *Nature* 610 (2022) 296–301.
- [2] J. Wei, K. Xiao, Y. Chen, X.P. Guo, B. Huang, Z.Q. Liu, In situ precise anchoring of Pt single atoms in spinel Mn<sub>3</sub>O<sub>4</sub> for a highly efficient hydrogen evolution reaction, *Energy Environ. Sci.* 15 (2022) 4592–4600.
- [3] X. Li, J. Hu, T. Yang, X. Yang, J. Qu, C.M. Li, Efficient photocatalytic H<sub>2</sub>-evolution coupled with valuable furfural-production on exquisite 2D/2D LaVO<sub>4</sub>/g-C<sub>3</sub>N<sub>4</sub> heterostructure, *Nano Energy* 92 (2022) 106714.
- [4] J. Wu, Z. Liu, X. Lin, E. Jiang, S. Zhang, P. Huo, Y. Yan, P. Zhou, Y. Yan, Breaking through water-splitting bottlenecks over carbon nitride with fluorination, *Nat. Commun.* 13 (2022) 6999.
- [5] W. Wang, L. Du, R. Xia, R. Liang, T. Zhou, H.K. Lee, Z. Yan, H. Luo, C. Shang, D. L. Phillips, Z. Guo, In situ protonated-phosphorus interstitial doping induces long-lived shallow charge trapping in porous C<sub>3</sub>-N<sub>4</sub> photocatalysts for highly efficient H<sub>2</sub> generation, *Energy Environ. Sci.* 16 (2023) 460–472.
- [6] S. Wu, H. Yu, S. Chen, X. Quan, Enhanced photocatalytic H<sub>2</sub>O<sub>2</sub> production over carbon nitride by doping and defect engineering, *ACS Catal.* 10 (2020) 14380–14389.
- [7] Y. Yuan, W.L. Wang, Z.W. Wang, J. Wang, Q.Y. Wu, Single-atom Ag-loaded carbon nitride photocatalysts for efficient degradation of acetaminophen: the role of Ag-atom and O<sub>2</sub>, *J. Environ. Sci.* 139 (2024) 12–22.
- [8] F.K. Kessler, Y. Zheng, D. Schwarz, C. Merschmann, W. Schnick, X. Wang, M. J. Bojdys, Functional carbon nitride materials-design strategies for electrochemical devices, *Nat. Rev. Mater.* 2 (2017) 17030.

- [9] M. Makaremi, S. Grixti, K.T. Butler, G.A. Ozin, C.V. Singh, Band engineering of carbon nitride monolayers by N-type, P-type, and isoelectronic doping for photocatalytic applications, *ACS Appl. Mater. Interfaces* 10 (2018) 11143–11151.
- [10] X.F. Zhou, J. Luo, B. Jin, Z.J. Wu, S.Y. Yang, S.S. Zhang, Y.H. Tian, Y.P. Fang, Y. G. Hou, X.S. Zhou, Sustainable synthesis of low-cost nitrogen-doped-carbon coated  $\text{Co}_3\text{W}_3\text{C}$ @ $\text{g-C}_3\text{N}_4$  composite photocatalyst for efficient hydrogen evolution, *Chem. Eng. J.* 426 (2021) 131208.
- [11] X.F. Zhou, L.Z. Peng, L.M. Xu, J. Luo, X.M. Ning, X.Q. Zhou, F. Peng, X.S. Zhou, Pd (II), Pt(II) metallosupramolecular complexes as single-site co-catalyst for photocatalytic  $\text{H}_2$  evolution, *Chem. Eng. J.* 474 (2023) 145967.
- [12] X.N. Yu, S.F. Ng, L.K. Putri, L.L. Tan, A.R. Mohamed, W.J. Ong, Point-defect engineering: leveraging imperfections in graphitic carbon nitride ( $\text{g-C}_3\text{N}_4$ ) photocatalysts toward artificial photosynthesis, *Small* 17 (2021) 2006851.
- [13] Y. Li, Z. He, L. Liu, Y. Jiang, W.J. Ong, Y. Duan, W. Ho, F. Dong, Inside-and-out modification of graphitic carbon nitride ( $\text{g-C}_3\text{N}_4$ ) photocatalysts via defect engineering for energy and environmental science, *Nano Energy* 105 (2023) 108032.
- [14] G. Liu, M. Xue, Q. Liu, H. Yang, Y. Zhou, Carbon doped honeycomb-like graphitic carbon nitride for photocatalytic hydrogen production, *J. Colloid Interface Sci.* 552 (2019) 728–734.
- [15] M.A. Mohamed, M.F.M. Zain, L. Jeffery Minggu, M.B. Kassim, N.A. Saidina Amin, W.N.W. Salleh, M.N.I. Salehmin, M.F. Md Nasir, Z.A. Mohd Hir, Constructing biotemplated 3D porous microtubular C-doped  $\text{g-C}_3\text{N}_4$  with tunable band structure and enhanced charge carrier separation, *Appl. Catal. B Environ.* 236 (2018) 265–279.
- [16] R. Gusmão, M. Veselý, Z. Sofer, Recent developments on the single atom supported at 2D materials beyond graphene as catalysts, *ACS Catal.* 10 (2020) 9634–9648.
- [17] J.B. Xi, H.S. Jung, Y. Xu, Xiao, F.J.W. Bae, S. Wang, Synthesis strategies, catalytic applications, and performance regulation of single-atom catalysts, *Adv. Funct. Mater.* 13 (2021) 2008318.
- [18] M.Y. Gao, F.Y. Tian, X. Zhang, Y.Q. Liu, Z.Y. Chen, Y.S. Yu, W.W. Yang, Y.L. Hou, Fast Charge separation and transfer strategy in polymeric carbon nitride for efficient photocatalytic  $\text{H}_2$  evolution: coupling surface schottky junctions and interlayer charge transfer channels, *Nano Energy* 103 (2022) 107767.
- [19] M. Ren, X.Y. Zhang, Y.Q. Liu, G. Yang, L. Qin, J.Q. Meng, Y.H. Guo, Y.X. Yang, Interlayer palladium-single-atom-coordinated cyano-group-rich graphitic carbon nitride for enhanced photocatalytic hydrogen production performance, *ACS Catal.* 12 (2022) 5077–5093.
- [20] Y. Huang, D. Li, Z. Fang, R. Chen, B. Luo, W. Shi, Controlling carbon self-doping site of  $\text{g-C}_3\text{N}_4$  for highly enhanced visible-light-driven hydrogen evolution, *Appl. Catal. B Environ.* 254 (2019) 128–134.
- [21] C. Wan, L. Zhou, L. Sun, L. Xu, D.G. Cheng, F. Chen, X. Zhan, Y. Yang, Boosting visible-light-driven hydrogen evolution from formic acid over AgPd/2D  $\text{g-C}_3\text{N}_4$  nanosheets mott-schottky photocatalyst, *Chem. Eng. J.* 396 (2020) 125229.
- [22] C. Ding, X. Lu, B. Tao, L. Yang, X. Xu, L. Tang, H. Chi, Y. Yang, D.M. Meira, L. Wang, X. Zhu, S. Li, Y. Zhou, Z. Zou, Interlayer spacing regulation by single-atom indium $^{+/-}\text{N}_4$  on carbon nitride for boosting  $\text{CO}_2/\text{CO}$  photo-conversion, *Adv. Funct. Mater.* (2023) 2302824.
- [23] S. Hu, P. Qiao, X. Yi, Y. Lei, H. Hu, J. Ye, D. Wang, Selective photocatalytic reduction of  $\text{CO}_2$  to CO mediated by silver single atoms anchored on tubular carbon nitride, *Angew. Chem. Int. Ed.* 62 (2023) e202304585.
- [24] L. Chen, H. Li, H. Li, H. Li, W. Qi, Q. Zhang, J. Zhu, P. Zhao, S. Yang, Single-atom engineering of directional charge transfer channels and active sites for photocatalytic hydrogen evolution, *Adv. Funct. Mater.* 28 (2018) 1802169.
- [25] X. Zhang, P. Ma, C. Wang, L. Gan, X. Chen, P. Zhang, Y. Wang, H. Li, L. Wang, X. Zhou, K. Zheng, Unraveling the dual defect sites in graphite carbon nitride for ultra-high photocatalytic  $\text{H}_2\text{O}_2$  evolution, *Energy Environ. Sci.* 15 (2022) 830–842.
- [26] W. Li, Z. Wei, K. Zhu, W. Wei, J. Yang, J. Jing, D.L. Phillips, Y. Zhu, Nitrogen-defect induced trap states steering electron-hole migration in graphite carbon nitride, *Appl. Catal. B Environ.* 306 (2022) 121142.
- [27] S.W. Cao, H. Li, T. Tong, H.C. Chen, A.C. Yu, J.G. Yu, H.M. Chen, Accelerating photogenerated charge kinetics via the  $\text{g-C}_3\text{N}_4$  schottky junction for enhanced visible-light-driven  $\text{CO}_2$  reduction, *Appl. Catal. B Environ.* 318 (2022) 121863.
- [28] Y. Xu, M. Fan, W. Yang, Y. Xiao, L. Zeng, X. Wu, Q. Xu, C. Su, Q. He, Homogeneous carbon/potassium-incorporation strategy for synthesizing red polymeric carbon nitride capable of near-infrared photocatalytic  $\text{H}_2$  production, *Adv. Mater.* 33 (2021) 2101455.
- [29] Y. Jiang, Z. Lin, Y. Zhang, Y. Lai, D. Liang, C. Yang, Facile synthesis of porous C-doped  $\text{C}_3\text{N}_4$ : fast charge separation and enhanced photocatalytic hydrogen evolution, *New J. Chem.* 44 (2020) 17891–17898.
- [30] T. Huang, S.G. Pan, L.L. Shi, A.P. Yu, X. Wang, Y.S. Fu, Hollow porous prismatic graphitic carbon nitride with nitrogen vacancies and oxygen doping: a high-performance visible light-driven catalyst for nitrogen fixation, *Nanoscale* 12 (2020) 1833–1841.
- [31] J. Wu, N. Li, X.H. Zhang, H.B. Fang, Y.Z. Zheng, X. Tao, Heteroatoms binary-doped hierarchical porous  $\text{g-C}_3\text{N}_4$  nanobelts for remarkably enhanced visible-light-driven hydrogen evolution, *Appl. Catal. B Environ.* 226 (2018) 61–70.
- [32] J. Sun, Y. Fu, G. He, X. Sun, X. Wang, Green suzuki-miyaura coupling reaction catalyzed by palladium nanoparticles supported on graphitic carbon nitride, *Appl. Catal. B Environ.* 165 (2015) 661–667.
- [33] F. Shao, Y. Gao, W. Xu, F. Sun, L. Chen, F. Li, W. Liu, Catalytic activation of formic acid using Pd nanocluster decorated graphitic carbon nitride for diclofenac reductive hydrodechlorination, *J. Hazard. Mater.* 446 (2023) 130677.
- [34] M. Lei, Y. Tang, H. Wang, L. Zhu, G. Zhang, Y. Zhou, H. Tang, A catalytic strategy for rapid cleavage of C–Cl bond under mild conditions: effects of active hydrogen induced by Pd nanoparticles on the complete dechlorination of chlorobenzenes, *Chem. Eng. J.* 419 (2021) 129510.
- [35] F. Guo, H. Zhang, H. Li, Z. Shen, Modulating the oxidative active species by regulating the valence of palladium cocatalyst in photocatalytic degradation of ciprofloxacin, *Appl. Catal. B Environ.* 306 (2022) 121092.
- [36] X.Y. Zhang, G. Yang, J.Q. Meng, L. Qin, M. Ren, Y. Pan, Y.X. Yang, Y.X. Guo, Acetamide- or formamide-assisted in situ approach to carbon-rich or nitrogen-deficient graphitic carbon nitride for notably enhanced visible-light photocatalytic redox performance, *Small* 19 (2023) 2208012.
- [37] J. Liu, Y. Yu, R.L. Qi, C.Y. Cao, X.Y. Liu, Y.J. Zheng, W.G. Song, Enhanced electron separation on in-plane benzene-ring doped  $\text{g-C}_3\text{N}_4$  nanosheets for visible light photocatalytic hydrogen evolution, *Appl. Catal. B Environ.* 244 (2019) 459–464.
- [38] H. Luo, T.S. Shan, J.W. Zhou, L.L. Huang, L.H. Chen, R.J. Sa, Y.S. Yamauchi, J. You, Y. Asakura, Z.H. Yuan, H. Xiao, Controlled synthesis of hollow carbon ring incorporated  $\text{g-C}_3\text{N}_4$  tubes for boosting photocatalytic  $\text{H}_2\text{O}_2$  production, *Appl. Catal. B Environ.* 337 (2023) 122933.
- [39] C. Han, P. Meng, E.R. Waclawik, C. Zhang, X.H. Li, H. Yang, M. Antonietti, J. Xu, Palladium/graphitic carbon nitride ( $\text{g-C}_3\text{N}_4$ ) stabilized emulsion microreactor as a store for hydrogen from ammonia borane for use in alkene hydrogenation, *Angew. Chem. Int. Ed.* 57 (2018) 14857–14861.
- [40] A. Li, E. Kan, S. Chen, Z. Du, X. Liu, T. Wang, W. Zhu, H. Huo, J. Ma, D. Liu, L. Song, H. Feng, M. Antonietti, J. Gong, Enabling high loading in single-atom catalysts on bare substrate with chemical scissors by saturating the anchoring sites, *Small* 18 (2022) 2200073.
- [41] Y. Yao, G. Ren, Z. Li, H. Bai, X. Hu, X. Meng, Nitrogen vacancy-induced deposition of Pd nanoparticles onto  $\text{g-C}_3\text{N}_4$  with greatly improved photocatalytic activity in  $\text{H}_2$  evolution, *Sol. RRL* 5 (2021) 2100145.
- [42] S. Zhou, L. Shang, Y. Zhao, R. Shi, G.I.N. Waterhouse, Y.C. Huang, L. Zheng, T. Zhang, Pd single-atom catalysts on nitrogen-doped graphene for the highly selective photothermal hydrogenation of acetylene to ethylene, *Adv. Mater.* 31 (2019) 1900509.
- [43] P. Liu, Z. Huang, X. Gao, X. Hong, J. Zhu, G. Wang, Y. Wu, J. Zeng, X. Zheng, Synergy between palladium single atoms and nanoparticles via hydrogen spillover for enhancing  $\text{CO}_2$  photoreduction to  $\text{CH}_4$ , *Adv. Mater.* 34 (2022) 2200057.
- [44] Y. Yang, Y. Guo, F. Liu, X. Yuan, Y. Guo, S. Zhang, W. Guo, M. Huo, Preparation and enhanced visible-light photocatalytic activity of silver deposited graphitic carbon nitride plasmonic photocatalyst, *Appl. Catal. B Environ.* 142 (2013) 828–837.
- [45] X.H. Wang, H. Yang, A. Meng, Z.J. Li, L.N. Yang, L. Wang, S.X. Li, G.C. Li, J. F. Huang, Interfacial engineering improved internal electric field contributing to direct Z-scheme-dominated mechanism over CdSe/SL-ZnIn<sub>2</sub>S<sub>4</sub>/MoSe<sub>2</sub> heterojunction for efficient photocatalytic hydrogen evolution, *Chem. Eng. J.* 431 (2022) 134000.
- [46] P.F. Xia, M. Antonietti, B.C. Zhu, T. Heil, J.G. Yu, S.W. Cao, Designing defective crystalline carbon nitride to enable selective  $\text{CO}_2$  photoreduction in the gas phase, *Adv. Funct. Mater.* 29 (2019) 1900093.
- [47] H.H. Zhai, P.F. Tan, M. Jiang, M.Y. Zhang, R.F. Ren, R.J. Sa, J. Pan, Electronic regulation of Pt single-atom catalysts via local coordination state adjustment for enhanced photocatalytic performance, *ACS Catal.* 13 (2023) 8063–8072.
- [48] L. Xu, B. Tian, T. Wang, Y. Yu, Y. Wu, J. Cui, Z. Cao, J. Wu, W. Zhang, Q. Zhang, J. Liu, Z. Li, Y. Tian, Direct Z-scheme polymeric heterojunction boosts photocatalytic hydrogen production via a rebuilt extended  $\pi$ -delocalized network, *Energy Environ. Sci.* 15 (2022) 5059–5068.
- [49] B.C. Qiu, L.J. Cai, N. Zhang, X.M. Tao, Y.A. Chai, Ternary dumbbell structure with spatially separated catalytic sites for photocatalytic overall water splitting, *Adv. Sci. J.* 7 (2020) 1903568.
- [50] D. Sun, Y.J. Chen, X.Y. Yu, Y.J. Yin, G.H. Tian, Engineering high-coordinated cerium single-atom sites on carbon nitride nanosheets for efficient photocatalytic amine oxidation and water splitting into hydrogen, *Chem. Eng. J.* 462 (2023) 142084.
- [51] M.Y. Gao, F.Y. Tian, X. Zhang, Y.Q. Liu, Z.Y. Chen, Y.S. Yu, W.W. Yang, Y.L. Hou, Fast charge separation and transfer strategy in polymeric carbon nitride for efficient photocatalytic  $\text{H}_2$  evolution: coupling surface Schottky junctions and interlayer charge transfer channels, *Nano Energy* 103 (2022) 107767.
- [52] Y.N. Hu, S. Zhang, Z.D. Zhang, H.X. Zhou, B. Li, Z.Y. Sun, X.M. Hu, W.X. Yang, X. Y. Li, Y. Wang, S.H. Liu, D.S. Wang, J. Lin, W.X. Chen, S. Wang, Enhancing photocatalytic-transfer semi-hydrogenation of alkynes over Pd/ $\text{g-C}_3\text{N}_4$  through dual regulation of nitrogen defects and the Mott–Schottky effect, *Adv. Mater.* 35 (2023) 2304130.
- [53] Y.X. Yang, Y.N. Guo, F.Y. Liu, X. Yuan, Y.H. Guo, S.Q. Zhang, W. Guo, M.X. Huo, Preparation and enhanced visible-light photocatalytic activity of silver deposited graphitic carbon nitride plasmonic photocatalyst, *Appl. Catal. B Environ.* 142 (2013) 828–837.